HAL
open science

Bubble Entrapment Condition in Bingham Materials

Lucas H.P. Deoclecio, Edson J. Soares, Hiranya Deka, Jean-Lou Pierson

To cite this version:

Lucas H.P. Deoclecio, Edson J. Soares, Hiranya Deka, Jean-Lou Pierson. Bubble Entrapment Condition in Bingham Materials. Journal of Non-Newtonian Fluid Mechanics, 2021, 295, pp.104616. 10.1016/j.jnnfm.2021.104616 . hal-03433192

HAL Id: hal-03433192

https://ifp.hal.science/hal-03433192v1

Submitted on 17 Nov 2021

HAL is a multi-disciplinary open access archive for the deposit and dissemination of scientific research documents, whether they are published or not. The documents may come from teaching and research institutions in France or abroad, or from public or private research centers.

L'archive ouverte pluridisciplinaire **HAL**, est destinée au dépôt et à la diffusion de documents scientifiques de niveau recherche, publiés ou non, émanant des établissements d'enseignement et de recherche français ou étrangers, des laboratoires publics ou privés.

Bubble Entrapment Condition in Bingham Materials

Lucas H. P. Deoclecio[a], Edson J. Soares[a], Hiranya Deka[b], Jean-Lou Pierson[b]

[a] *LABREO, Department of Mechanical Engineering, Universidade Federal do Espirito Santo, Avenida Fernando Ferrari, 514, Goiabeiras, 29075-910, ES, Brazil*

[b] *IFP Energies nouvelles, Solaize 69360, France*

Abstract

We investigate the entrapment condition of initially spherical and ellipsoidal bubbles in viscoplastic materials using direct numerical simulations. For a spherical bubble, the entrapment condition depends on the balance between the buoyancy force and the yield stress of the viscoplastic material. For non-spherical bubbles, interfacial tension may yield the surrounding material to minimize the surface energy of the bubble. The yielding of the surrounding material also facilitates the rising motion of the bubble owing to buoyancy. However, the bubble gets entrapped later if the stress exerted by buoyancy force is less than the yield stress of the material. We evaluate the yield-stress parameter for different bubble shapes and physical parame-ters, and predict the critical yield-stress parameter for the entrapment of a bubble. The effect of the viscosity ratio on the bubble entrapment condition is also investigated.

Keywords: Viscoplastic liquids; Bubble entrapment; Yield-stress parameter.

Email addresses: `edson.soares@ufes.br` (Edson J. Soares), `+55 27 33579500 5028` (Edson J. Soares)

1. Introduction

Bubble rise in a viscous liquid is a fundamental problem in fluid mechanics. The problem is also important from the industrial application point of view. In many applications, the surrounding is a viscoplastic fluid such as processed foods, cosmetics, medicines, crude oil, to name a few (Tripathi et al., 2015; Potapov et al., 2006; Sikorski et al., 2009). Understanding the bubble rise dynamics through a viscoplastic material is of utmost importance for the optimization of these industrial processes.

The first concept of viscoplastic fluid was proposed by Bingham (1922) who states that viscoplastic materials behave like a solid when applied stress is below the limit called yield stress, and behave like a fluid when the applied stress is higher than the yield stress. Viscoplastic materials may entrap bubbles indefinitely when the buoyant force is not sufficient to overcome the material yield stress. Depending on the application, bubble entrapment may be desirable or undesirable. For example, bubble mobility is desirable in water treatment and fermentation, where its mobility may influence gas diffusion, and consequently the efficiency of physical and chemical processes. On the other hand, bubble entrapment is desirable in food processing, such as chocolate, ketchup, and mayonnaise, in order to improve its taste. Bubble entrapment is also desirable in the processing of cosmetics such as hair gels and shampoos. A small amount of bubbles is also allowed in cement to improve workability and freeze-thaw resistance, at the expense of reduced compressive strength and concrete blisters. There are also situations in which the presence of bubbles may be dangerous, as in the blowout of oil wells and

the processing of solid fuels. Therefore, the entrapment condition of bubbles in viscoplastic materials is of great interest.

The mobility of viscous drops and solid spheres through a viscoplastic material also caught the attention of the community (Holenberg et al., 2011; Beris et al., 1985). Beris et al. (1985) studied the motion of a solid sphere through a viscoplastic material and defined the yield-stress parameter Y_g which is the ratio of yield strength and external force acting on the sphere. In the case of free-falling solid sphere where the external force is gravity, Y_g can be written as

$$Y_g = \frac{3}{2}\frac{\tau_y}{R\Delta\rho g}, \tag{1}$$

where τ_y is the yield stress of the viscoplastic fluid, $\Delta\rho$ is the density difference between the fluid and the solid particle, g is the acceleration due to gravity, and R is the sphere radius. The authors estimated that the critical value of the yield-stress parameter Y_{gc} for the entrapment of solid spheres is approximately 0.143. If $Y_g < Y_{gc}$, the particle moves, otherwise it is trapped by the yield stress. The experimental data of Tabuteau et al. (2007) support the prediction of Beris et al. (1985).

Later, the researchers investigating the rise of a bubble on a viscoplastic fluid adapted the definition of Y_g as the ratio of yield strength to the buoyancy force exerted by the bubble. Several attempts have been made to find the critical yield stress parameter using theoretical (Dubash and Frigaard, 2004), experimental (Dubash and Frigaard, 2007; Sikorski et al., 2009; Lopez et al., 2018), and numerical (Tsamopoulos et al., 2008; Dimakopoulos et al., 2013) tools. Using the theory of variational principles, Dubash and Frigaard

(2004) estimated the value of Y_{gc} as 0.866 for spherical bubbles. However, the same authors later reported that this prediction provides sufficient but not necessary conditions for bubble entrapment (Dubash and Frigaard, 2007). The theoretical studies are performed using simplified assumptions, such as predefined bubbles and yield surface shapes, and predefined velocity field (Dubash and Frigaard, 2004; Wang et al., 2019; Lou et al., 2020).

The entrapment condition is also expressed as a function of Bingham number in a few earlier studies (Dubash and Frigaard, 2004, 2007; Tsamopoulos et al., 2008; Dimakopoulos et al., 2013), where the characteristic strain rate of the Bingham number is calculated from the buoyancy effect. Indeed, the Bingham number is nothing but the yield stress parameter Y_g of Eq. (1) without a factor of 3/2. Sikorski et al. (2009) reported that the equivalent radius of the bubble is not the best suitable length scale in the case of a deformed bubble. They used the radius of the maximum cross-sectional plane normal to the flow, R_{max}, to calculate the value of Y_g. Since Y_g is a representation of the ratio between the yield stress to the buoyant stress, the authors defined Y_g as

$$Y_g = \frac{3}{2}\frac{R_{max}^2 \tau_y}{R^3 \Delta\rho g}. \tag{2}$$

The equivalent radius of a spherical bubble was used in the denominator to express the buoyancy force, whereas maximum radius, R_{max}, was used in the numerator to find the resistance offered by the yield stress. This parameter differs from Y_g given in Eq. (1) by a factor of $(R_{max}/R)^2$. Sikorski et al. (2009) estimated this critical parameter from their experimental results as $Y_{gc} \leq 0.50 \pm 0.04$. However, the experimental data of Lopez et al. (2018) esti-

mates the value of Y_{gc} to be approximately 0.13 using the definition Eq. (2), and varying in between 0.15 to 0.45 when using the definition Eq. (1). This dramatic difference between the two experimental observations is not clear and might be a consequence of experimental condition or change in other rheological properties as the concentration of the Carbopol suspension was not the same. The difficulties involved in the experimental characterization of real fluids make such investigations very complex and challenging (Dubash and Frigaard, 2007; Frey et al., 2015; Lopez et al., 2018; Pourzahedi et al., 2021).

Numerical simulation of bubble rise in a viscoplastic medium is also challenging because of the discontinuous viscosity function. Moreover, the yield region and bubble shape need to be determined as a part of the solution. Tsamopoulos et al. (2008) obtained steady-state solutions for the rising of bubbles in a Bingham fluid using the Papanastasio model (PM) (Papanastasiou, 1987). They reported that the critical entrapment limit, Y_{gc}, varies from 0.214 to 0.321 as a monotonic function of the Bond number Bo ($=\rho_1 g R^2/\sigma$), where ρ_1 is the density of the viscoplastic material and σ is the surface tension coefficient. The regularized viscosity models allow creeping flow in the unyielded zone and one needs to be careful in finding the entrapment condition. As explained in Tsamopoulos et al. (2008), the criteria based on second invariant of the stress tensor ($\|\tau\| \leq \tau_y$ for unyielded material and $\|\tau\| > \tau_y$ for yielded material) provides a better interpretation of the results. Dimakopoulos et al. (2013) compared the earlier results of Tsamopoulos et al. (2008) with steady-state solutions using the Augmented Lagrangian Method (ALM). They found that the entrapment criteria given by Tsamopoulos et al.

(2008) gave a good estimative of the entrapment condition when the regularization parameters were high. Also, they studied the rising of bubbles in both Herschel-Bulkley and Bingham fluids and reported that the entrapment conditions are independent of the consistency and power-law indexes of the fluid. The entrapment condition depends on τ_y which is in agreement with Dubash and Frigaard (2004). Their results show that Y_{gc} varies in the range $0.194-0.217$ but the increase is not a monotonic function of the Bo. First Y_{gc} increases with an increase in Bo, and later, Y_{gc} starts decreasing with the increase in Bo. These results were obtained using a steady-state ALM formulation and the computational cost in ALM is high. Later, Dimakopoulos et al. (2018) proposed a numerical method called the Penalized Augmented Lagrangian Method (PALM) which has shown to be a fast converging and efficient algorithm compared to ALM and is capable of tracking the yield surface and predicting the flow field of viscoplastic fluids accurately. Tripathi et al. (2015) performed transient numerical simulations using the volume of fluid method and demonstrated that in large yield stress and weak surface tension regime, the bubble rise is transient (or oscillating). Tsamopoulos et al. (2008) reported that the ratio between Y_{gc} for spherical bubbles (in-finitesimal viscosity ratio) and solid spheres (infinite viscosity ratio) is equal to 1.5, the same ratio of the terminal velocity of a solid sphere to that of a spherical bubble under the same buoyancy force. However, they did not make any comment on the entrapment condition at the intermediate viscosity ratio.

Despite the abundance of literature on the topic, there are many challenges which are far from being completely understood, especially the depen-

dence of the value of the critical yield-stress parameter (Y_{gc}) on the initial shape of the bubble and the viscosity ratio. We attempt to understand the condition for bubble entrapment in a viscoplastic fluid using time-dependent numerical simulations. The Bingham model is used to mimic the yield stress characteristics of the viscoplastic material. The rest of the paper is organized as follows. Section 2 describes the problem formulation, where the computational domain, boundary conditions, governing equations, and dimensionless numbers are presented followed by validation of the numerical model. In Sec. 3, the results are presented and discussed. Finally, we draw up the conclusions in Sec. 4.

2. Problem Formulation

We investigate the entrapment condition of spherical and deformed bubbles in a Bingham material using direct numerical simulations in an axisymmetric geometry. In this section, first, we present the computational domain along with the boundary and initial conditions. Then we present the governing equations and the important dimensionless parameters. Finally, we present the validation tests performed to check the solver accuracy and grid dependency.

2.1. Computational domain

A representative diagram of the computational domain is shown in Fig. 1. Axisymmetric simulations are performed in a cylindrical coordinate system (r, z) where the axis of symmetry lies along the z-axis (the right boundary). The simulations are performed in a square domain of height $H = 25\,D$, where D is the equivalent diameter of a spherical bubble having the same volume

as that of the bubble. The origin of the coordinate system lies at the bottom right corner of the domain as shown in Fig. 1. At the start of the simulations, the bubble center is located at a distance $z_i = 5\,D$ from the origin. The computational domain is sufficiently large to avoid any boundary effects. The surrounding viscoplastic fluid (represented as Fluid 1) is modeled using the Bingham constitutive equations while the bubble (represented as Fluid 2) is a Newtonian fluid. Gravity acts on the negative z-direction. Initially, both fluids are at rest. We have initialized the bubble with different aspect ratios a/b (a is the axis length in the z-direction and b is axis length in the r direction) in the range 0.5 to 2.0. In Fig. 1, the bubble aspect ratio is equal to 1 corresponding to a sphere ($a = b = D$). We apply free-slip boundary conditions with no mass penetration for the velocity field at the bottom, left, and top boundaries. The Neumann boundary condition for the pressure field is applied at these boundaries.

2.2. Governing equations

In the present simulations, the fluids are considered incompressible. The governing mass and momentum conservation equations are given as

$$\nabla \cdot \mathbf{u} = 0, \tag{3}$$

$$\rho \left[\frac{\partial \mathbf{u}}{\partial \mathbf{t}} + \mathbf{u} \cdot \nabla \mathbf{u} \right] = -\nabla P + \nabla \cdot \left[\mu \left(\nabla \mathbf{u} + \nabla \mathbf{u}^{\mathbf{T}} \right) \right] + \mathbf{f}_\sigma - \rho \mathbf{g}. \tag{4}$$

Here, $\mathbf{u}$ (u_r, u_z) is the velocity field, where u_r and u_z are the velocity components in the radial (r) and axial (z) directions, respectively; P is the pressure

field; $\mathbf{g} = g\mathbf{e_z}$ where g is the the acceleration due to gravity and $\mathbf{e_z}$ is the unit vector in the z-direction; ρ is the density field; μ is the viscosity field; t is time; $\mathbf{f}_\sigma$ is the local density of capillary force per unit volume and is equal to $\mathbf{f}_\sigma = \sigma\kappa\mathbf{n}\delta_\mathbf{s}$ where σ is the surface tension coefficient, κ is the mean curvature of the interface, δ_s is the Dirac delta function which is zero everywhere except at the interface and $\mathbf{n}$ is the unit normal to the interface.

Here, the bulk fluid is viscoplastic (Fluid 1) and the bubble is a Newtonian fluid (Fluid 2). The respective densities of the two fluids ρ_1 and ρ_2 are constants. The viscosity μ_2 of the bubble is constant while the viscosity of the bulk viscoplastic phase μ_1 is modeled using the regularized version of the Bingham constitutive law given as (Bingham, 1922; Frigaard and Nouar, 2005; Allouche et al., 2000; Balmforth et al., 2014)

$$\mu_1 = \mu_p + \frac{\tau_y}{\|\dot{\gamma}\| + \epsilon}. \tag{5}$$

Here, μ_p is the plastic viscosity of the viscoplastic material; τ_y is the yield stress of the viscoplastic material; $\|\dot{\gamma}\| = \sqrt{(1/2)\dot{\boldsymbol{\gamma}}\colon\dot{\boldsymbol{\gamma}}}$is the Frobenius norm of the strain rate tensor, $\dot{\boldsymbol{\gamma}}$. The regularization parameter ϵ is calculated as

$$\epsilon = \frac{\tau_y}{N\mu_c}, \tag{6}$$

where $\mu_c = \mu_p + \tau_y/\dot{\gamma}_c$ is the characteristic viscosity based on the characteristic strain rate $\dot{\gamma}_c$ (defined later) and N is a dimensionless parameter whose value is large. We carry out a convergence test to optimize the value of N which is presented in Sec. 2.4.

The two phases are separated by the volume fraction α whose value is taken as 1 and 0 for fluid 1 and fluid 2, respectively. The advection equation

for the volume fraction field is solved to track the interface separating the two fluids.

$$\frac{\partial \alpha}{\partial t} + \mathbf{u} \cdot \nabla \alpha = \mathbf{0} \tag{7}$$

The density ρ and viscosity μ are then calculated based on volume fraction in each grid cell as

$$\rho = \rho_1 \alpha + \rho_2 (1 - \alpha), \tag{8}$$

$$\mu = \frac{1}{\frac{\alpha}{\mu_1} + \frac{1-\alpha}{\mu_2}}. \tag{9}$$

We consider harmonic mean for viscosity since in the case of high-viscosity contrast, the harmonic mean of viscosity work better than the arithmetic mean (Tryggvason et al., 2011). We have tested the simulations for both means which are presented in Sec. 2.4. We do not observe any considerable difference in the simulation results except the solution/convergence time. The yielded (unyielded) regions are separated based on the von Mises criterion given as $\|\tau\| > \tau_y$ ($\|\tau\| \leq \tau_y$), where $\|\tau\|$ is the magnitude of the deviatoric stress tensor.

2.3. Non-dimensional parameters

The following scalings are used to non-dimensionalize the governing equations and boundary conditions:

$$\begin{aligned} &(\bar{r}, \bar{z}) = (r/D, z/D), \bar{\mathbf{u}} = \mathbf{u}/U,\ \bar{t} = t/t_c,\ \bar{P} = P/\rho_1 U^2, \\ &\bar{\mu} = \mu/\mu_c,\ \bar{\rho} = \rho/\rho_1,\ \bar{\dot{\boldsymbol{\gamma}}} = \dot{\boldsymbol{\gamma}}/\dot{\gamma}_c \end{aligned} \tag{10}$$

The characteristics velocity U is defined as $U = \sqrt{(\rho_1 - \rho_2) g D / \rho_1}$, the characteristic time t_c is defined as $t_c = D/U$, the characteristic strain rate $\dot{\gamma}_c$ is defined as $\dot{\gamma}_c = 1/t_c = U/D$, and the characteristic viscosity μ_c is defined

as $\mu_c = \mu_p + \tau_y/\dot{\gamma}_c$. It is worth noting that μ_c includes the contribution of the yield-stress, as recommended by Thompson and Soares (2016). Using this scaling we get the following dimensionless parameters that describe the problem of interest.

$$
\begin{aligned}
Ar &= \sqrt{\rho_1 \Delta\rho g D^3}/\mu_c, \\
Bo &= \Delta\rho g D^2/\sigma, \\
Pl &= \tau_y/(\tau_y + \mu_p \dot{\gamma}_c), \\
\mu_r &= \mu_2/\mu_c, \\
\rho_r &= \rho_2/\rho_1.
\end{aligned}
$$

The Archimedes number, Ar, represents the relative importance of the buoyancy force to the viscous force, while the Bond number, Bo, represents the relative importance of the buoyancy force to the capillary force. The Plastic number, Pl, indicates the plastic nature of the fluid and its value ranges from 0 to 1. $Pl = 0$ indicates that the yield stress is zero (Newtonian fluid) while $Pl = 1$ indicates that the fluid is completely plastic (infinite yield stress) and remains undeformed. Since the viscosity of Fluid 1 is not constant, we define the viscosity ratio, μ_r, as the viscosity of Fluid 2 over the characteristic viscosity, μ_c. The density ratio $\rho_r = \rho_2/\rho_1$ is fixed (=0.01) in all the simulations.

The momentum equation can be represented in terms of these dimensionless parameters as

$$\bar{\rho}\left[\frac{\partial \bar{\mathbf{u}}}{\partial \bar{t}} + \bar{\mathbf{u}} \cdot \nabla \bar{\mathbf{u}}\right] = -\nabla \bar{P} + \frac{1}{Ar}\nabla \cdot \left[\bar{\mu}\left(\nabla \bar{\mathbf{u}} + \nabla \bar{\mathbf{u}}^T\right)\right] + \frac{1}{Bo}\bar{\kappa}\mathbf{n}\delta_s - \bar{\rho}\mathbf{e_z}. \quad (11)$$

In Eq. (11), the Plastic number is hidden inside the term $\bar{\mu} = 1/(\alpha/\bar{\mu}_1 + (1-\alpha)/\bar{\mu}_2)$ where the $\bar{\mu}_1$ is given as

$$\bar{\mu}_1 = \frac{\mu_1}{\mu_c} = (1 - Pl)\left[1 + \frac{Pl}{(1 - Pl)(\bar{\dot{\gamma}} + \frac{Pl}{N})}\right]. \tag{12}$$

2.4. Code validation

The numerical simulations are performed using the open-source solver *Basilisk* (Basilisk; Popinet, 2009, 2015; Lagrée et al., 2011). The viscoplastic model of Basilisk solver has been successfully used for complex flows by different researchers (Lagrée et al., 2011; Deka et al., 2019, 2020).

The mesh is dynamically adapted as a function of the volume fraction, the velocity field, and the yield surface. Figure 2 exemplifies how the mesh is adapted, where the image has been mirrored on the z-axis. All simulations start with a uniform mesh of refinement level[1] 6 in the whole domain, with local refinement around the bubble at the maximum level as shown in Fig. 2 (a). In Fig. 2 (a), the maximum refinement level is 12. Figure 2 (b) shows the dynamically adapted mesh at $\bar{t} = 10.0$ for the same condition presented by Dimakopoulos et al. (2013), $Ar = 33.33$, $Bo = 200$, $Pl = 0.83$, $\mu_r = 0$ and $\rho_r = 0$ (the viscosity and density of the gas phase in the bubble were neglected). It can be seen in Fig. 2 (b) that the mesh is refined at the bubble interface, on the yield surface, and on the regions where there is a velocity gradient.

The dimensionless velocity profile of the bubble center of mass with dimensionless time is shown in Fig. 3 for maximum mesh refinement level of

[1]The number of cells per dimension is given by 2^n, where n is level of refinement. For example, if a 2D square domain is discretized with a refinement level 8, each direction will contain 256 cells, then the whole domain will contain 65,536 cells.

9, 10, 11, 12, and 13 with $N = 10^6$ considering the harmonic mean of viscosity (continuous lines) and one case with the arithmatic mean of viscosity (dashed line). The minimum level for dynamic mesh adaption is kept constant at level 4. It can be seen in Fig. 3 that the velocity profile does not change considerably when changing the maximum level of refinement from 12 to 13; however, the computational time increases considerably. Additionally, a mesh maximum refinement level of either 9, 10, or 11 does not capture the fluids interface accurately (a skirt forms in the bubble back). Hence, a maximum refinement level of 12 is chosen to perform the numerical simulations. We did not observe any effect of the minimum refinement level on the flow field. It is also evident in Fig. 3 that the velocity profile is in good agreement for both harmonic and arithmetic mean of viscosity implying that the results are almost independent of the way the jump of viscosity is computed. The maximum refinement level in the simulations (level 12) corresponds to a cell size of approximately $6.103 \times 10^{-3}\, D$.

Next, we check the value of N to optimize the computational time without compromising the accuracy. Figure 4 presents the bubble shape (red line), yielded (white) and unyielded (black) regions for $N = 10^3, 10^4, 10^5$, and 10^6. For $N = 10^6$ the external yield surface is in qualitative agreement with the predictions of Beris et al. (1985) (Figure 1 of authors). The velocity profile of the bubble center of mass with time is shown in Fig. 5 for different values of N. Since the result with $N = 10^6$ does not change much from the result with $N = 10^7$, whether the computational time is higher in the later we perform the simulations with $N = 10^6$.

Finally, we validate the solver by reproducing the experimental results of

Wegener et al. (2010) for Newtonian fluids. The terminal velocity of toluene drops of different diameters rising in water is calculated and compared with the experiments. We observe a very good agreement between the simulation results and experiments as depicted in Fig. 6. The decrease in terminal velocity after a maximum velocity is due to changes in the drop shape. We also reproduce the steady-state solution of Dimakopoulos et al. (2013) (Fig. 7), who simulated rising bubbles using the Augmented Lagrangian Method to model the Bingham fluid. The dimensionless parameters are $Bo = 200$, $Ar = 33.33$, $Pl = 0.83$, $\mu_r = 0.001$ and $\rho_r = 0.01$. As evident in Fig. 7, the agreement with the ALM is reasonable for both yielded/unyielded region and the bubble shape. It is to be noted that our definitions of Bo and Ar differ from that of Dimakopoulos et al. (2013) since we use the bubble diameter instead of its radius. Moreover, our representation of Archimedes number is the square root of the one considered by them. Furthermore, we define the Archimedes number based on $\mu_c = \mu_p + \tau_y/\dot{\gamma}_c$ to include the yield-stress contribution on viscosity while Dimakopoulos et al. (2013) used μ_p.

3. Results and discussion

In this section, we discuss the entrapment condition of spherical and non-spherical bubbles. We cover a wide range of the governing dimensionless parameters in numerical simulations. First, we discuss the entrapment criteria used to find whether a bubble is static or mobile.

3.1. Bubble entrapment criteria

We consider that the bubble is mobile when a complete envelope of yielded material appears around it. This is similar to the criteria proposed by

Tsamopoulos et al. (2008) who considered that the bubble is arrested when the external yield surface merges with the unyielded material around the bubble equator. In order to determine the critical Plastic number Pl_c and the critical yield-stress parameter Y_{gc} for bubble entrapment, we employ a method similar to the root-finding Bisection method. We vary Pl in discrete intervals for a given Ar until the difference between the minimum value of the Plastic number for which the bubble is static, and the maximum value for which the bubble is mobile is less the 5 %. Pl_c is taken as the average of these two values, and it has an error margin of about $\pm 2.5\,\%$.

Figure 9 shows the bubble interface and the yielded/unyielded regions for $Ar = 5$, $Bo = 1$, $\mu_r = 0.001$ and $Pl = 0.25$, 0.32, 0.33 and 0.34 at $\bar{t} = 0.2$. The initial shape of the bubbles is spherical. At this particular instant, although the bubbles have not reached a steady state, the development of a complete (Fig. 9(a) and (b)) or an incomplete (Fig. 9 (c) and (d)) envelop of yielded material is clearly visible. For low values of Pl, the yielded envelope spans far from the bubble surface (Fig. 9 (a)), and as Pl increases, the yielded envelope size decreases and an unyielded region appears on the bubble equator (Fig. 9 (b)). The gap between the unyielded material on the bubble equator and the outer unyielded surface decreases with the increase in Pl. At large Pl, the outer and the equatorial unyielded surfaces merge indicating no resultant movement of the bubble (Fig. 9 (c)), although yielded regions are found above and below the bubble (which are expected to be oscillation effect). If Pl is increased further, no yielded region is observed around the bubble (Fig. 9 (d)). We do not see any considerable change of the yielded regions with time. Therefore, Figs. 9 (a) and (b) depict two rising bubbles,

while Fig. 9 (c) and (d) depict two static bubbles. For this special case, the maximum value of Pl for which the bubble is mobile and the minimum value of Pl for which the bubble is static are 0.32 and 0.33, respectively, and therefore we interpret the critical plastic number as $Pl_c = 0.325$.

3.2. Entrapment condition of spherical bubbles

The driving force for bubble rising is the buoyancy force, and the energy budget for the work done by this force is shared among the yield stress, viscosity, surface tension, and inertia. For an entrapped spherical bubble, the buoyancy force is not able to overcome the resistance of the yield stress. Therefore, it is expected that the entrapment condition for a spherical bubble is governed solely by the yield-stress parameter, Y_g, which may be written as $Y_g = 3Pl/Ar$. The critical yield-stress parameter Y_{gc} may also depend on μ_r, as demonstrated by Tsamopoulos et al. (2008) and Sikorski et al. (2009) for bubbles (zero viscosity ratio) and solid particles (infinite viscosity ratio). Moreover, according to Tsamopoulos et al. (2008) and Dimakopoulos et al. (2013), Y_{gc} varies with Bo. However, in their work, every entrapped bubble had a different shape and the change in Y_{gc} could also be due to the bubble shape. Therefore, we perform a systematic investigation to know the Bond number and the viscosity ratio effects for bubbles of the same initial shape. We present and discuss our results for spherical bubbles in the present section and for non-spherical bubbles in Section 3.3.

We first construct a critical entrapment map for spherical bubbles as a function of $P\,l$ and Ar, with the former ranging from 0.01 to 0.96, and the latter ranging from 0.1 to 15. For a given Ar, if $Pl > Pl_c$, where $Pl_c(Ar)$ is the critical Plastic number for bubble entrapment, the bubble is static,

otherwise it will rise. For $Pl = 0.0$, the surrounding fluid is Newtonian and bubbles will always move, and, for $Pl = 1.0$ the material behaves like a solid and the bubbles do not move. In between these two limits, we find the critical Y_{gc}. Here, the Bond number is set as 1, and the viscosity and density ratios are set as 0.001 and 0.01, respectively. Figure 10 shows the results of the numerical simulation in a $Pl - Ar$ map. Here, the green squares represent mobile bubbles while the red squares represent entrapped bubbles. The boundary between the entrapped and mobile regimes can be represented by a linear relationship of Pl and Ar, given by $Y_{gc} = 3Pl_c/Ar \approx 0.195$. Since the bubbles are spherical, calculating Y_{gc} using either Eq. (1) or Eq. (2) gives the same result.

The critical Y_{gc} as a function of Ar is plotted in Fig. 11 for $Bo = 1$ and $\mu_r = 0.001$ along with several other data obtained from the literature. Our results agree with that of Dimakopoulos et al. (2013) and Tsamopoulos et al.(2008) who extimated the values of Y_{gc} as 0.196 and 0.210, respectively. Both results are for $Bo \ll 1$, and therefore, it is expected that the bubbles have a spherical shape. The numerical results deviate from the theoretical prediction of Dubash and Frigaard (2004) ($Y_{gc} = 0.87$) and experimental results of Sikorski et al. (2009) ($Y_{gc} = 0.50$) and Lopez et al. (2018) ($Y_{gc} = 0.13$). The bubbles are non-spherical in the experiments of Sikorski et al. (2009) and Lopez et al. (2018) and Y_{gc} is calculated using Eq. 2. We have already mentioned that the discrepancy between the two experimental investigations may be because of the difficulties in the experimental characterization of the rheological properties. The discrepancy may also come owing to the difficulties in estimating the entrapment condition experimentally. The real

fluids also have elastic characteristics. Recently, Pourzahedi et al. (2021) have demonstrated that the geometrical differences of the bubble shape in the experiments (Sikorski et al., 2009; Lopez et al., 2018) and numerical simulations (Tsamopoulos et al., 2008; Dimakopoulos et al., 2013) come from the elastic nature of fluid which is not present in the simple rheological models considered in the numerical simulations. Our numerical model also does not consider the elastic nature of the fluid. Nevertheless, the data obtained from the present computations as well as from the literature suggest that Y_{gc} is independent of Ar for spherical bubbles.

To check the effect of the Bond number, we perform numerical simulations by changing the value of Bo for a spherical bubble. The simulations are performed for $Bo = 0.01$, 0.1, 100, 250 and 1000, $Ar = 1$ and 5, and $\mu_r = 0.001$. Figure 12 presents Y_{gc} as a function of Bo for $Ar = 1$ and 5, along with the results of Tsamopoulos et al. (2008) and Dimakopoulos et al. (2013). The average value of Y_{gc} in the present simulations is approximately 0.200 with a maximum deviation of 10 %. Such a small variation of Y_{gc} over five orders of magnitude variation of Bo suggests that Y_{gc} barely depends on the Bo for a spherical bubble. The larger deviation of Y_{gc} in Tsamopoulos et al. (2008) is therefore expected to be because of the change in the shape of the bubble.

Figure 13 shows the variation of Y_{gc} as a function of μ_r. The simula-tions are performed for three values of $Ar = 1$, 5, and 10 and $Bo = 1$. To understand the viscosity ratio effect we perform the simulation for different viscosity ratios: $\mu_r = 0.001$, 0.01, 0.1, 1, 10, 20, 50, 100, 150 and 200. The critical yield stress parameter Y_{gc} decreases with the increase in the viscosity

ratio. However, the decrease is very small for lower values of viscosity ratios. For instance, Y_{gc} change from 0.194 to 0.191 when μ_r is changed from 0.001 to 10, which is negligibly small compared to the four orders of magnitude variation of μ_r. However, the critical yield-stress parameter decreases considerably at higher viscosity ratios. For $\mu_r = 50$, the Y_{gc} value is approximately 0.177 and 0.180 for $Ar = 10$ and 5, respectively. The change in the Y_{gc} is a result of the change in the interfacial stress at the surface of the bubble as the bubble becomes more rigid at a higher viscosity ratio. With further increase in the viscosity ratio ($\mu_r = 200$ in our simulations), the critical value of Y_{gc} approaches the asymptotic limit 0.143, which is the yield stress parameter for a rigid solid sphere reported in Beris et al. (1985).

The above parametric study suggests that, for a spherical bubble, the entrapment condition primarily depends on competition between the buoyancy and yield stress. If the buoyancy force is not sufficient to overcome the yield stress, a spherical bubble will remain entrapped. The critical value of the yield stress parameter Y_{gc} for the entrapment of a spherical bubble is approximately constant at lower viscosity ratio ($Y_{gc} \approx 0.20 \pm 0.02$). At a higher viscosity ratio, the critical yield stress parameter decreases and approaches the asymptotic limit of Y_{gc} for a solid sphere.

3.3. Entrapment condition of non-spherical bubbles

For non-spherical bubbles, there are two possibilities: first, if the surface tension force is strong enough it will deform the bubble and will try to bring the bubble to the spherical shape, and second, if the surface tension is weak, there will be no deformation of the bubble because of surface tension. In the first case, even though the buoyancy force is not enough to overcome the

yield stress, surface tension may yield the surrounding material to bring the bubble to a spherical shape similar to that reported in Deka et al. (2020) for slender drops. Therefore, the critical Y_{gc} depends on Bo for non-spherical bubbles, unlike the spherical bubbles where critical Y_{gc} was found to be independent of Bo. Moreover, the viscosity may also play a significant role as it resists the shape-change motion of bubble. We perform numerical sim-ulations to assess the entrapment condition of non-spherical bubbles of the same volume by considering different aspect ratios. First, we study bubble entrapment condition in low surface tension regime which is presented in Sec. 3.3.1. In this regime, the surface tension force is not strong enough to yield the surrounding material. Next, in Sec. 3.3.2, we discuss the bubble mobility in higher surface tension regimes where surface tension overcomes the yield stress. Finally, we discuss the viscosity ratio effect on the mobility of the bubbles in Sec. 3.3.3.

3.3.1. Low surface tension regime

First, we investigate the bubble entrapment in the low surface tension regime. We consider a typical case with $Bo = 100$, $Ar = 5$ and $\mu_r = 0.001$. Figure 14 presents the critical yield-stress parameter for the non-spherical bubbles with aspect ratios of 0.5, 0.75, 1.0, 1.5, and 2.0, using Eq. (1) (blue line) and Eq. (2) (green line). Y_{gc} varies significantly according to Eq. (1), but remains approximately constant according to Eq. (2). Some earlier literature (Dubash and Frigaard, 2004, 2007; Tsamopoulos et al., 2008; Dimakopoulos et al., 2013) have used Eq. (1) (using the equivalent radius of the bubble) since it is easier to relate to the Bingham number when the deformation rate is expressed as a function of the buoyancy force. However, as pointed out by

Sikorski et al. (2009), the definition of Eq. (2) is more relevant since the stress exerted by the bubble to yield the surrounding viscoplastic material depends on the area normal to the direction of the buoyancy force. Indeed, when using the definition of Eq. (1), Lopez et al. (2018) estimated Y_{gc} to vary between 0.15 and 0.45, while using the definition of Eq. (2) the authors estimated a single value of Y_{gc} of approximately 0.13. This corroborates that, in the low surface tension regime, the plasticity required to hold a non-spherical bubble is a function of the net buoyancy force as well as the bubble shape. The critical Y_{gc} in Fig. 14 obtained from Eq. (2) is approximately 0.2 which is same as that obtained for spherical bubbles in proceeding section.

3.3.2. High surface tension regime

In a high surface tension regime, surface tension force may yield the surrounding material to bring the bubble to a spherical shape from a deformed shape to minimize the surface energy. The yielding of the surrounding material by the surface tension force also facilitates the rising motion of the bubble as buoyancy force is continuously acting on it. Figures 15 (a) and (b) present typical snapshots of initially ellipsoidal bubbles of aspect ratios of 2.0 and 0.5 at $\bar{t}$ = 0.0, 0.2, 0.4, 0.6 and 0.8. The dimensionless parameters are Bo = 1, Ar = 5, $P\,l$ = 0.33, and μ_r = 0.001. For the same values of Ar, $P\,l$ and aspect ratio, but for Bo = 100, a initially prolate bubble ($Y_g \approx 0.125$ using Eq. (2)) is mobile, while an oblate bubble ($Y_g \approx 0.315$ using Eq. (2)) is static (not shown). This is because surface tension is too weak to yield the surrounding material and the mobility of the bubble depends on the balance between buoyancy and yield stress. For Bo = 1, surface tension yields the surrounding material to pull back the bubbles towards a spherical

shape. As the surrounding material is yielded, the bubbles also start rising because of buoyancy. When the bubbles approach a spherical shape, the surface tension effect on the yielding of the surrounding material vanishes, and the entrapment condition depends on the competition between buoyancy and yield stress. The maximum value of Pl for which the bubble is mobile in the later stage is approximately 0.33 in both cases, which is very close to the critical limit for an initially spherical bubble ($Pl_c \approx 0.32$). This suggests that if surface tension is strong enough to yield the surrounding material by minimizing the surface energy, the critical entrapment condition of oblate and prolate bubbles is nearly equal to that of an initially spherical bubble. A small difference appears because the non-spherical bubble does not necessarily take an exact spherical shape in the later stage. Depending on the final shape of the bubble, the critical Plastic number may vary slightly (also evident in Refs. (Tsamopoulos et al., 2008; Dimakopoulos et al., 2013))

Figures 16 (a) and (b) show the temporal variation of the aspect ratio and the dimensionless rise velocity of a bubble, respectively. The dimensionless parameters are $\mu_r = 0.001$, $Ar = 5$, $Pl = 0.33$, $Bo = 0.1$ and 1, and $a/b = 0.5$ and 2.0. Because of high surface tension ($Bo = 0.1$ and 1) force, the bubble shape changes towards a spherical one. The bubble velocity first increases and then decreases, and finally approaches zero. This is because the Pl value is close to the entrapment condition. It is evident that for $Bo = 0.1$, the bubbles oscillate (between oblate and prolate shapes), while for $Bo = 1$, the bubble shape smoothly changes to a nearly spherical shape.

The effective buoyant stress depends on the cross-section area normal to the direction of buoyancy force. For an oblate bubble, the cross-sectional area

normal to buoyancy force is higher which reduces the effective buoyant stress, whereas for a prolate bubble, it is opposite. As a result, we see an oblate bubble is entrapped while the prolate bubble was mobile in the weak surface tension regime ($Bo = 100$). If the surface tension force is strong enough to yield the surrounding material, an oblate bubble may begin to rise. For instance, for an oblate bubble of aspect ration 0.5, $Bo = 0.1$, and $Ar = 5$, surface tension yields the surrounding material to approach a spherical shape and the yielding of surrounding material also facilitates the rising motion of the bubble. The bubble may get entrapped later when it reaches a nearly spherical shape. The critical Plastic number, in this case, is approximately 0.335. On the other hand, for $Bo = 100$, the critical Plastic number of an oblate bubble with of aspect ratio of 0.5 is approximately 0.215. The weak surface tension force (Bo =100) is not able to yield the surrounding material, which is the reason for the lower value of the critical Plastic number. The Pl_c lies between 0.335 and 0.215 for an oblate bubble of aspect ratio 0.5 when the Bo is varied between 0.1 and 100.

In the case of an initially prolate bubble of aspect ratio 2.0 with $Ar = 5$, $Bo = 100$, the critical value is $Pl_c \approx 0.515$. If the Bo is changed to 0.1, the bubble starts moving initially, but gets entrapped later even for $Pl_c < 0.515$. The critical Plastic number for permanent movement of the bubble in this case (Bo =0.1) is approximately 0.335. Thus we see that the when surface tension effect becomes strong (lower Bo), the critical plastic number for a prolate bubble decreases while the critical plastic number for an oblate bubble increases. We discuss this in more detail in the succeeding part.

A prolate bubble may start rising due to the yielding of the surrounding

material by the surface tension force or by buoyancy, but may get entrapped later because its maximum cross-sectional area normal to the buoyancy force increases. The increase of cross-sectional area reduces the effective buoyant stress induced on the surrounding, and when this induced stress is lower than the yield stress the bubble gets entrapped. Thus, initially prolate bubbles may move momentarily or permanently depending on the surface tension force. For example, in Figure 15 (a), if $P\,l$ were equal to 0.35, the bubble would move only momentarily and no yielded material would be found around the bubble at $\bar{t} = 0.8$, while for $Pl = 0.33$ the bubble moves permanently.

On the other hand, in the case of an oblate-shaped bubble, surface tension reduces the maximum cross-sectional normal to the direction of buoyancy force. The reduction of the cross-sectional area normal to the direction of buoyancy force increases the effective buoyant stress, and hence allows the bubble to rise. Differently from prolate bubbles, besides being momentarily mobile, oblate bubbles may be momentarily static, depending on the surface tension force. For high surface tension regime, the initial surface tension pulling force is able to form a complete envelope of yielded material. If the buoyant stress is sufficient to yield the surrounding material the bubble rises, otherwise the bubble gets entrapped. For example, in Figure 15 (b), if Pl were equal to 0.35, the bubble would move initially, but no yielded material would be found around the bubble at $\bar{t} = 0.8$. For $P\,l = 0.33$, the bubble moves permanently. For intermediate surface tension regime, surface tension slowly and partially yields the surrounding material. In has been observed that in this regime, for oblate bubbles, the upper surface of the bubble gets yielded, but some regions on the lower surface of the

bubble remain unyielded. Thus, the shape of the bubble changes without any net movement of the bubble. Eventually, as the bubble cross-sectional radius decreases, this momentarily static bubble is set into motion, as seen in Figure 15 (c), for $Bo = 10$, $Ar = 10$, $Pl = 0.60$, $\mu_r = 0.001$ and initial aspect ratio equal to 0.5. For higher values of Pl and/or μ_r (discussed in more detail in the next Sec. 3.3.3), unyielded material can still be found in lower surface of the bubble, even for later times, as shown in Figure 15 (d) for $\mu_r = 10$ anf $\bar{t}$ up to 40.0.

To get a better quantitative understanding, we plot the value of Pl_c and Y_{gc} for different Bo and aspect ratios. First, we try to find the value of Pl_c for the entrapment of a bubble that was initially set in motion by the surface tension force. Figure 17 (a) shows the Pl_c as function of Bo for $Ar = 5$ and 10, $\mu_r = 0.001$, and for $a/b = 0.50$, 0.75 and 2.00. It is evident in Fig. 17 (a) that as Bo decreases, the critical Plastic number approaches the value of a spherical bubble in the high surface tension regime (for $Bo \leq 5$ in our simulations). Increasing the Archimedes numbers shifts the Pl_c vs Bo curve upwards. For aspect ratios close to unity, Pl_c tends to be a constant with Bo for the low surface tension regime. For example, for $a/b = 0.75$, Pl_c is the same for $Bo = 25$, 50 and 100, while for $a/b = 0.50$, Pl_c increases as Bo decreases from 100 to 25. Present simulations suggest that, for a non-spherical bubble, the critical plastic number for bubble entrapment deviates from that of the spherical bubbles only if the Bo is high ($Bo > 5$ in the present study). Otherwise, the entrapment condition is approximately the same as that of a spherical bubble because of the high dominance of the surface tension force which eventually transforms the non-spherical shape

into a nearly spherical one. In the high Bo regime, the critical plastic number shows an increasing trend for a prolate bubble with the increase in Bo, while it shows a decreasing trend for an oblate bubble (Fig. 17 (a)). The reason for this opposite trend is the contrasting effect of surface tension on prolate and oblate bubbles in the change of the effective buoyant stress as discussed above.

The radius of the maximum normal plane of the bubble (normal to buoyancy) at the instant of entrapment is plotted in Fig. 17 (b). It is evident in Fig. 17 (b) that the curve of the maximum radius (or maximum cross-sectional area) for different initial aspect ratios converge to a single curve as the Bond number decreases. For the same initial aspect ratio ($a/b = 0.50$) and different Archimedes numbers ($Ar = 5$ and 10) the curves overlap in the whole range of Bond number considered here. This indicates that the maximum radius at the instant of entrapment is not a function of the Archimedes number; it depends on the initial aspect ratio and Bo. Fig. 17 (c) shows the variation of Y_{gc} (using Eq. 2 where R_{max} is obtained from Fig. 17 (b)) as a function of Bo. It is evident that the entrapment condition $Y_{gc} \approx 0.20 \pm 0.02$ (gray area) still holds for the permanent motion of the bubble for the whole range of Bo considered here. This illustrates that, regardless of the initial condition (a/b and Bo), the entrapment condition can be well specified by a constant value of Y_{gc} by properly defining the yield stress parameter Y_{gc} based on the final shape of the bubble.

3.3.3. Viscosity ratio effect on the entrapment condition of non-spherical bubbles

Viscous dissipation slows down the motion of a bubble from a non-spherical shape to a spherical shape. Surface tension tries to bring a de-formed bubble to a spherical shape and the increased viscosity of the bubble resists the motion. In the high surface regime ($Bo \ll 1$), the bubble reaches a spherical shape because of the strong dominance of capillary force. This is evident in Fig. 18 (a) where the variation is aspect ratio of an oblate bubble is shown at different viscosity ratios for $Bo = 0.1$ and $Pl = 0.66$. Increased viscosity also reduces the inertia effect and thus the oscillatory motion of the bubble. The final mobility of the bubble depends on the competition between the buoyancy and yield stress of the surrounding material.

Increasing the viscosity ratio decreases the maximum velocity of the bubble. This comes as a consequence of the slow shape-change motion of the bubble. The viscosity of the yielded regions of the viscoplastic material depends on the strain rate on the yielded region. At a higher strain rate, viscosity is low ($\mu_1 = \tau_y/\|\dot{\gamma}\| + \mu_p$). Because of the slow shape-change mo-tion of the bubble at a higher viscosity ratio, the strain rate on the yielded region is low resulting in a higher viscosity of the yielded material. This subsequently decreases the rising velocity of the bubble at a higher viscosity ratio as evident in Fig 18 (b). All bubble in Fig. 18 (a) and (b) are only momentarily mobile. As the figures show, for the range of viscosity ratio studied and for $Bo \ll 1$, increasing the viscosity ratio decrease the motion duration of momentarily mobile bubbles due to the higher viscosity of the viscoplastic surrounding material.

With the increase in Bo, the effect of the viscosity ratio becomes significant. In the low viscosity regime, the bubble reaches a spherical shape by yielding the surrounding material around it. At a higher viscosity ratio, the bubble can yield the surrounding material but slowly. As a result, a yielded envelope is not observed around the bubble. The region on the lower sur-face of the bubble remains unyielded and thus resists the rising motion of the bubble as evident in Fig. 15 (c) and (d) for $Bo = 10$, $P\,l = 0.60$ and $\mu_r = 0.001$ and 10, respectively. In the former, the bubble is momentarily entrapped, while in the latter the bubble is permanently entrapped.

Finally, we evaluate the critical plastic number and critical yield-stress parameter for the entrapment of a bubble at different viscosity ratios. The results are shown in Figs. 19 (a) and (b), respectively, for μ_r varying from 0.001 to 1. It is evident in Fig. 19 that neither the critical plastic number nor the yield-stress parameter change with the change in viscosity ratio. For $\mu_r = 10$, the value of $P\,l_c$ decreases in the intermediate Bond number regime. This is due to the increased resistance force of the bubble viscosity to shape change. For example, for $Bo = 10$ and $\mu_r = 0.001$, $P\,l_c \approx 0.615$, while for $\mu_r = 10$, $P\,l_c \approx 0.52$. However, the values of R_{max} for bubble mobility does not vary with μ_r. Hence, increasing the viscosity ratio decreases Y_{gc} for $\mu_r \gtrsim 10$. We may infer an opposite behaviour for prolate shaped bubble since viscosity ratio resists R_{max} increase. Edson ans Jean-Lou: I need more time to finish the simulations to determine $P\,l_c$ for $\mu_r = 10$ that I started last week, and thus, finish this last paragraph. These simulations should be finished while you two read the revised manuscript.

4. Concluding remarks

We have investigated the entrapment condition of initially spherical and non-spherical bubbles in a Bingham material. The entrapment condition can be expressed by a approximate value of the yield stress parameter Y_{gc} for both spherical and non-spherical bubbles in low viscosity ratio regimes given as $Y_{gc} \approx 0.20 \pm 0.02$.

For a spherical bubble, the entrapment condition is independent of the Bond number, for the whole range of Bo studied (0.1 to 1000), and the viscosity ratio for μ_r up to about 50. For $\mu_r \gtrsim 50$, Y_{gc} decreases with μ_r, until reaches the asymptotic values of 0.143 for solid particles at $\mu_r \approx 200$.

For initially non-spherical bubbles, the surface tension force plays an important role in the final entrapment condition in the intermediate surface tension regime ($5 \leq Bo \leq 50$). In the low surface tension regime, surface tension force does not play any role in the final entrapment condition of a non-spherical bubble. Here, the critical plastic number for entrapment in-creases as the shape changes from a prolate to an oblate shape because of the change in the effective area on which the force exerted by the yield stress acts. However, by defining the yield stress parameter, Y_{gc}, based on the radius of the maximum cross-sectional area of the bubble (normal to buoyancy), we observe an approximately constant value of Y_{gc}. In the high surface ten-sion regime, surface tension force completely yields the surrounding material around the bubble, making a non-spherical bubble rises while returning to a spherical shape, with the same entrapment criteria as that of a spherical bubble. In the intermediate regime, surface tension can yield the surround-ing material to reduce the deformation of the bubble and start its the rising

motion. However, the surface tension effect is not strong enough to convert the shape of the bubble into an exactly spherical one. Therefore, the bub-ble remains in a deformed stage. In this regime, the prolate-shaped bubbles have a slightly higher critical plastic number than the spherical bubbles, and may set into motion permanently or momentarily, depending on the balance between surface tension and yield stress. On the other hand, oblate-shaped bubbles have a slightly lower critical plastic number than the spherical bub-bles, and may be permanently or momentarily static, also depending on the balance between surface tension and yield stress.

(This last paragraph of the conclusion should change when I finish the last simulations). By appropriately defining the yield stress parameter based on the radius of the final maximum cross-sectional area of the bubble (normal to buoyancy), the entrapment criteria can be expressed as a constant value of the yield stress parameter given as $Y_{gc} = 0.20 \pm 0.02$. Present investigation reveals that viscosity ratio ($\mu_r \lesssim 10$) does not change the value of critical yield-stress parameter Y_{gc} for bubble entrapment. However, since the bubble viscosity resists deformation, the critical Plastic number is reduced with viscosity ratio increase for oblate bubbles in intermediate values of the Bond number. We may infer an opposite behaviour for prolate bubbles.

References

Allouche, M., Frigaard, I.A., Sona, G., 2000. Static wall layers in the displacement of two visco-plastic fluids in a plane channel. J. Fluid Mech. 424, 243–277.

Balmforth, N.J., Frigaard, I.A., Ovarlez, G., 2014. Yielding to stress: recent

developments in viscoplastic fluid mechanics. Annual Review of Fluid Mechanics 46, 121–146.

Basilisk, . URL: http://basilisk.fr/.

Beris, A., Tsamopoulos, J., Armstrong, R., Brown, R., 1985. Creeping motion of a sphere through a bingham plastic. Journal of Fluid Mechanics 158, 219–244.

Bingham, E.C., 1922. Fluidity and Plasticity. McGraw-Hill, New York.

Deka, H., Pierson, J.L., Soares, E.J., 2019. Retraction of a viscoplastic liquid sheet. Journal of Non-Newtonian Fluid Mechanics 272, 104172.

Deka, H., Pierson, J.L., Soares, E.J., 2020. Retraction criteria of viscoplastic drops and sheets: Long-wave approximations. Journal of Non-Newtonian Fluid Mechanics 284, 104352.

Dimakopoulos, Y., Makrigiorgos, G., Georgiou, G.C., Tsamopoulos, J., 2018. The pal (penalized augmented lagrangian) method for computing viscoplastic flows: A new fast converging scheme. Journal of Non-Newtonian Fluid Mechanics 256, 23–41.

Dimakopoulos, Y., Pavlidis, M., Tsamopoulos, J., 2013. Steady bubble rise in herschel–bulkley fluids and comparison of predictions via the augmented lagrangian method with those via the papanastasiou model. Journal of Non-Newtonian Fluid Mechanics 200, 34–51.

Dubash, N., Frigaard, I., 2004. Conditions for static bubbles in viscoplastic fluids. Physics of fluids 16, 4319–4330.

Dubash, N., Frigaard, I., 2007. Propagation and stopping of air bubbles in carbopol solutions. Journal of non-newtonian fluid mechanics 142, 123–134.

Frey, S.L., Naccache, M.F., de Souza Mendes, P.R., Thompson, R.L., dos Santos, D.D., Link, F.B., Fonseca, C., 2015. Performance of an elasto-viscoplastic model in some benchmark problems. Mechanics of Time-Dependent Materials 19, 419–438.

Frigaard, I., Nouar, C., 2005. On the usage of viscosity regularisation methods for visco-plastic fluid flow computation. Journal of non-newtonian fluid mechanics 127, 1–26.

Holenberg, Y., Lavrenteva, O.M., Nir, A., 2011. Interaction of viscous drops in a yield stress material. Rheologica acta 50, 375–387.

Lagrée, P.Y., Staron, L., Popinet, S., 2011. The granular column collapse as a continuum: validity of a two-dimensional navier-stokes model with a [mu](i)-rheology. Journal of Fluid Mechanics 686, 378.

Lopez, W.F., Naccache, M.F., de Souza Mendes, P.R., 2018. Rising bubbles in yield stress materials. Journal of Rheology 62, 209–219.

Lou, W., Wang, Z., Pan, S., Sun, B., Zhang, J., Chen, W., 2020. Prediction model and energy dissipation analysis of taylor bubble rise velocity in yield stress fluid. Chemical Engineering Journal , 125261.

Papanastasiou, T.C., 1987. Flows of materials with yield. J. Rheology 31, 385–404.

Popinet, S., 2009. An accurate adaptive solver for surface-tension-driven interfacial flows. Journal of Computational Physics 228, 5838–5866.

Popinet, S., 2015. A quadtree-adaptive multigrid solver for the serre–green–naghdi equations. Journal of Computational Physics 302, 336–358.

Potapov, A., Spivak, R., Lavrenteva, O.M., Nir, A., 2006. Motion and deformation of drops in bingham fluid. Industrial & engineering chemistry research 45, 6985–6995.

Pourzahedi, A., Zare, M., Frigaard, I., 2021. Eliminating injection and memory effects in bubble rise experiments within yield stress fluids. Journal of Non-Newtonian Fluid Mechanics 292, 104531.

Sikorski, D., Tabuteau, H., de Bruyn, J.R., 2009. Motion and shape of bubbles rising through a yield-stress fluid. J. Non-Newtonian Fluid Mech. 159, 10–16.

Tabuteau, H., Coussot, P., de Bruyn, J.R., 2007. Drag force on a sphere in steady motion through a yield-stress fluid. Journal of rheology 51, 125–137.

Thompson, R.L., Soares, E..J., 2016. Viscoplastic dimensionless numbers. Journal of Non-Newtonian Fluid Mechanics 241, 60–69.

Tripathi, M.K., Sahu, K.C., Karapetsas, G., Matar, O.K., 2015. Bubble rise dynamics in a viscoplastic material. Journal of Non-Newtonian Fluid Mechanics 222, 217–226.

Tryggvason, r., Scardovelli, R., Zaleski, S., 2011. Direct Numerical Sim-

ulations of Gas-Liquid Multiphase Flows. Cambridge University Press. doi:10.1017/CBO9780511975264.

Tsamopoulos, J., Dimakopoulos, Y., Chatzidai, N., Karapetsas, G., Pavlidis, M., 2008. Steady bubble rise and deformation in newtonian and viscoplastic fluids and conditions for bubble entrapment. Journal of Fluid Mechanics 601, 123.

Wang, Z., Lou, W., Sun, B., Pan, S., Zhao, X., Liu, H., 2019. A model for predicting bubble velocity in yield stress fluid at low reynolds number. Chemical Engineering Science 201, 325–338.

Wegener, M., Kraume, M., Paschedag, A.R., 2010. Terminal and transient drop rise velocity of single toluene droplets in water. AIChE journal 56, 2–10.

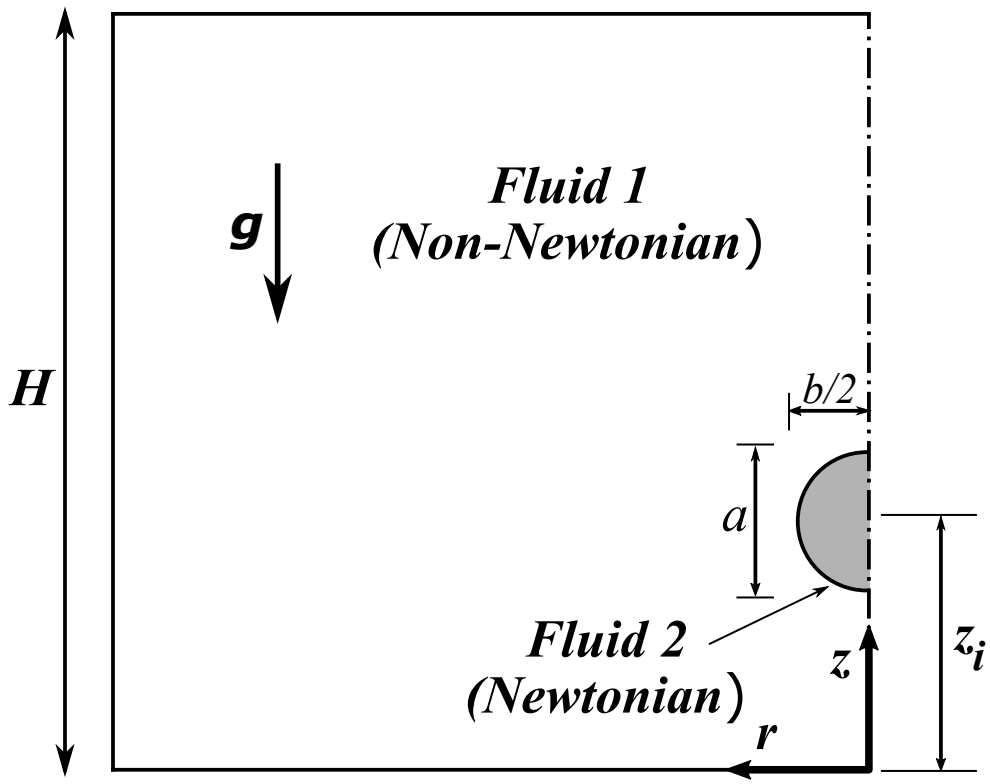

Figure 1: A representative diagram of the computational domain. A square domain of side length $H = 25D$ is considered to perform the numerical simulations, where D is the diameter of the bubble. The axisymmetric simulations are performed in a cylindrical coordinate system (r, z) where r and z are the axial and radial coordinates respectively. Gravity acts in the negative z-direction and, the bubble center is initially located at a height of $5D$ from the lower boundary. The surrounding is a viscoplastic fluid (fluid 1) and the bubble is a Newtonian fluid (fluid 2) of the bubble.

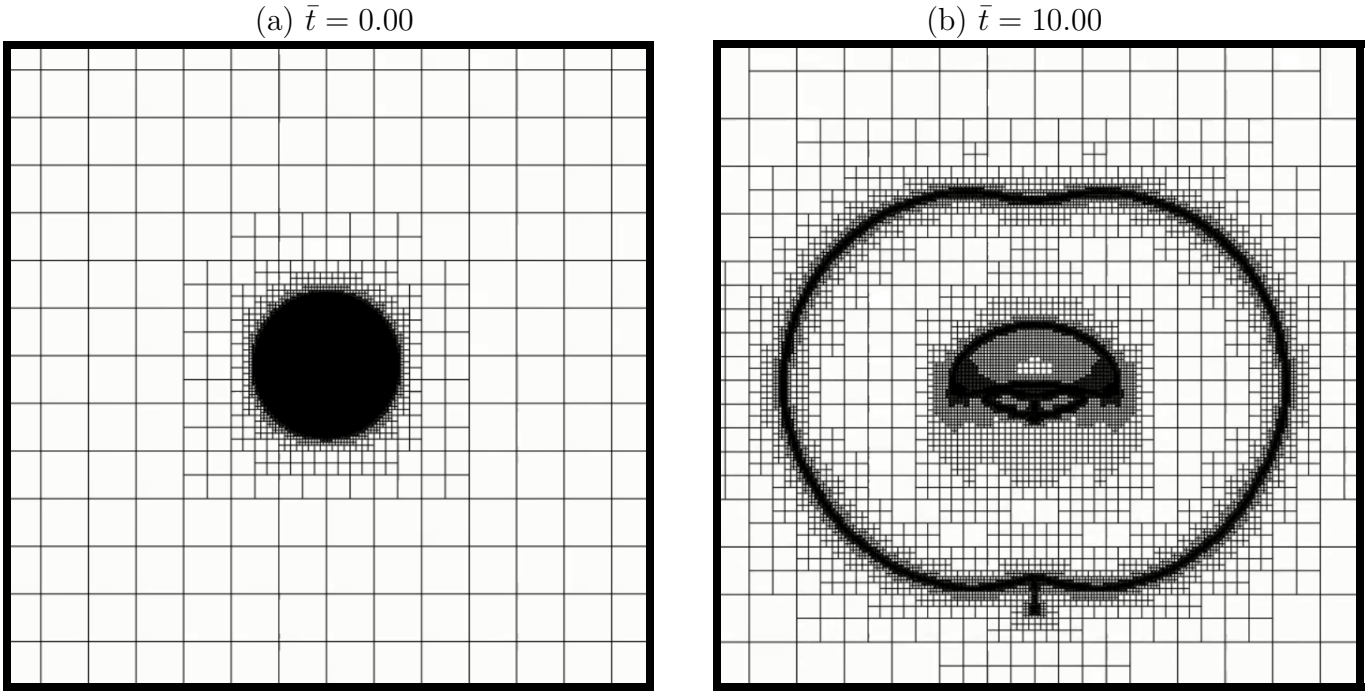

Figure 2: A view of the mesh at time $\bar{t} = 0.00$ (a) and $\bar{t} = 10.00$ (b), for $Ar = 33.33$, $Bo = 200.00$, and $Pl = 0.83$, with maximum level 12 and minimum level 4.

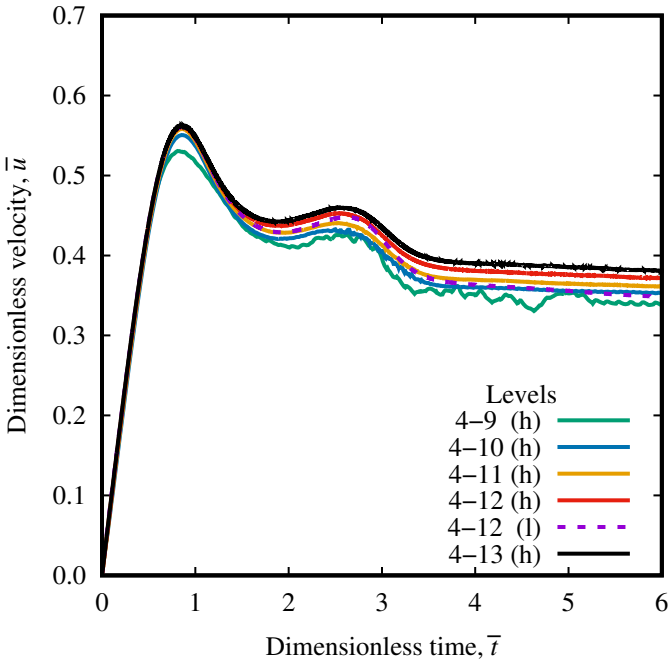

Figure 3: Dimensionless velocity, $\bar{u}$, of the center of mass versus dimensionless time, $\bar{t}$, for different mesh refinement levels. The minimum refinement level in all cases is 4 while the maximum refinement level is changed from 9 to 13. The simulations are performed considering the harmonic mean of viscosity and one case considering the arithmetic mean of viscosity (dashed line) is also shown for comparison. The dimensionless parameters are $Ar = 33.33$, $Bo = 200.00$, and $Pl = 0.83$.

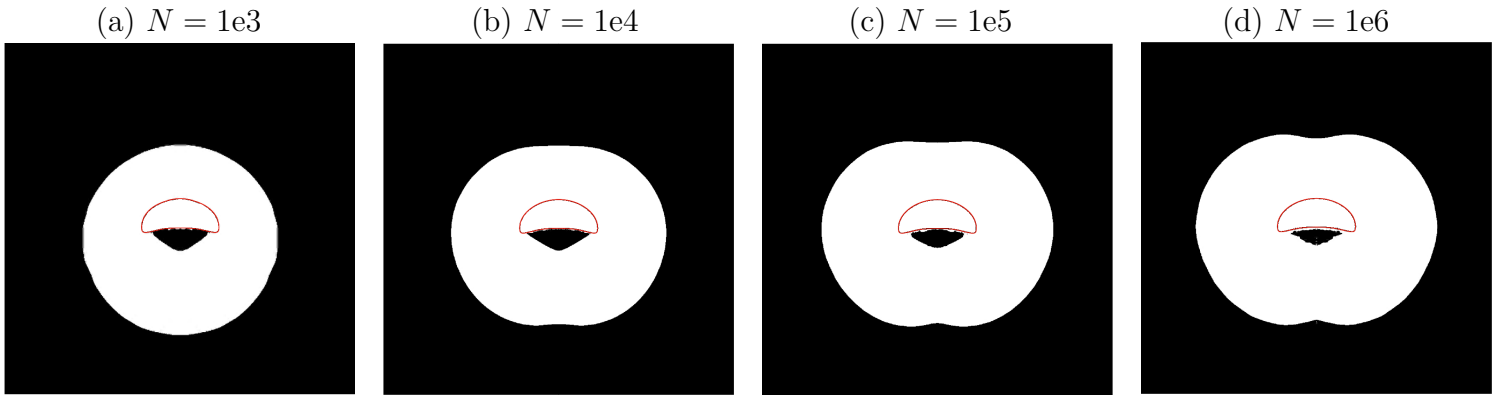

Figure 4: Snapshots of the yield (white)/unyielded (black) regions around the bubble along with bubble interface. The simulation results are shown for $N =$ (a) 10^3, (b) 10^4, (c) 10^5 and (d) 10^6 at $\bar{t} = 10.00$. The dimensionless parameters are $Ar = 33.33$, $Bo = 200.00$, and $Pl = 0.83$.

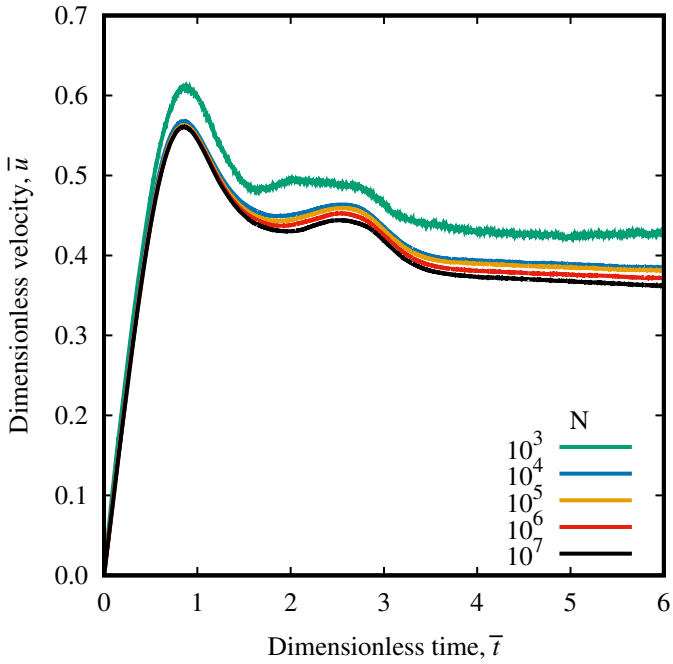

Figure 5: Dimensionless velocity $\bar{u}$ of the center of mass versus dimensionless time $\bar{t}$ for $N = 10^3$, 10^4, 10^5, 10^6 and 10^7, for $Ar = 33.33$, $Bo = 200.00$, and $Pl = 0.83$.

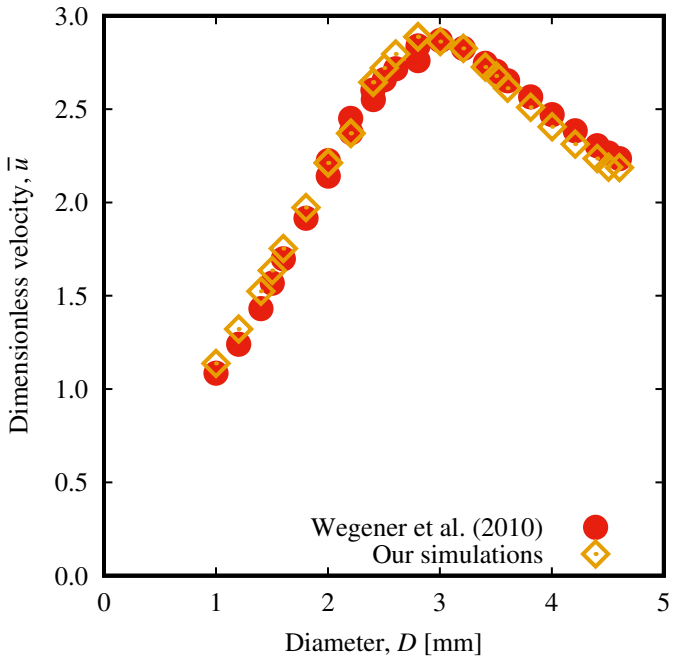

Figure 6: Comparison of dimensionless terminal velocity $\bar{u}_o$ obtained from present simulations with the experimental results of Wegener et al. (2010) for Newtonian bubbles rising in a Newtonian matrix.

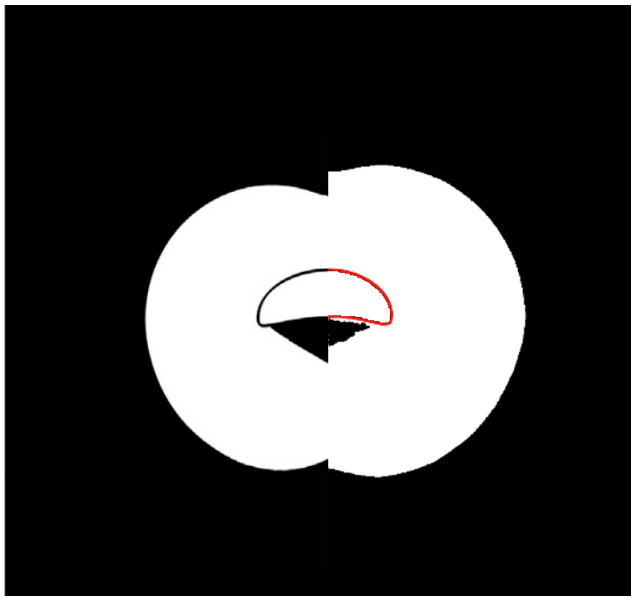

Figure 7: Comparison of present simulation result (right half) with the steady state result of Dimakopoulos et al. (2013) using the ALM (left half). The simulations are performed using $N = 10^6$ and at maximum refinement level 12.

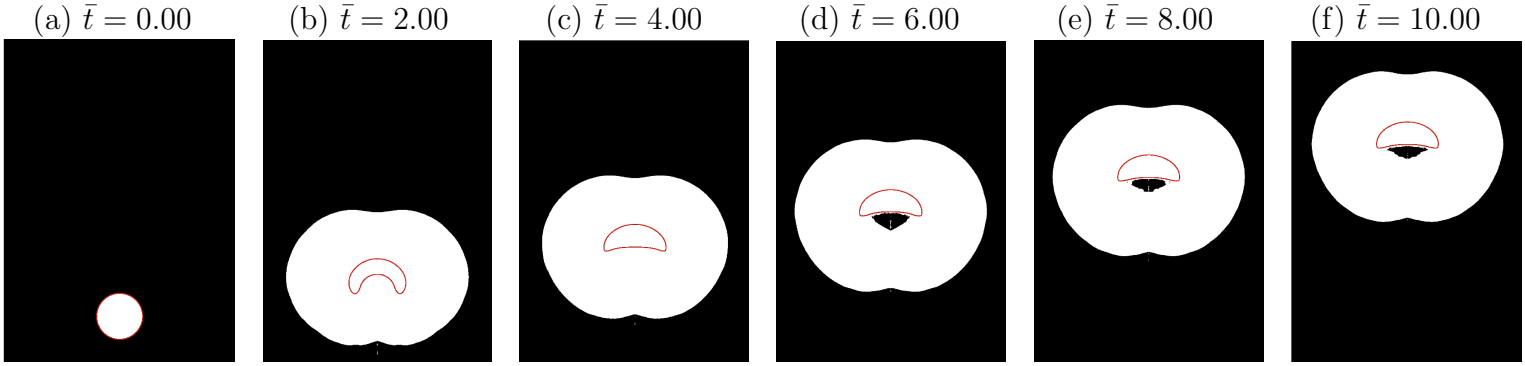

Figure 8: The interface of the bubble and the yielded(white)/unyielded(black) regions for $Ar = 33.33$, $Bo = 200.00$, and $Pl = 0.83$ at different time instants.

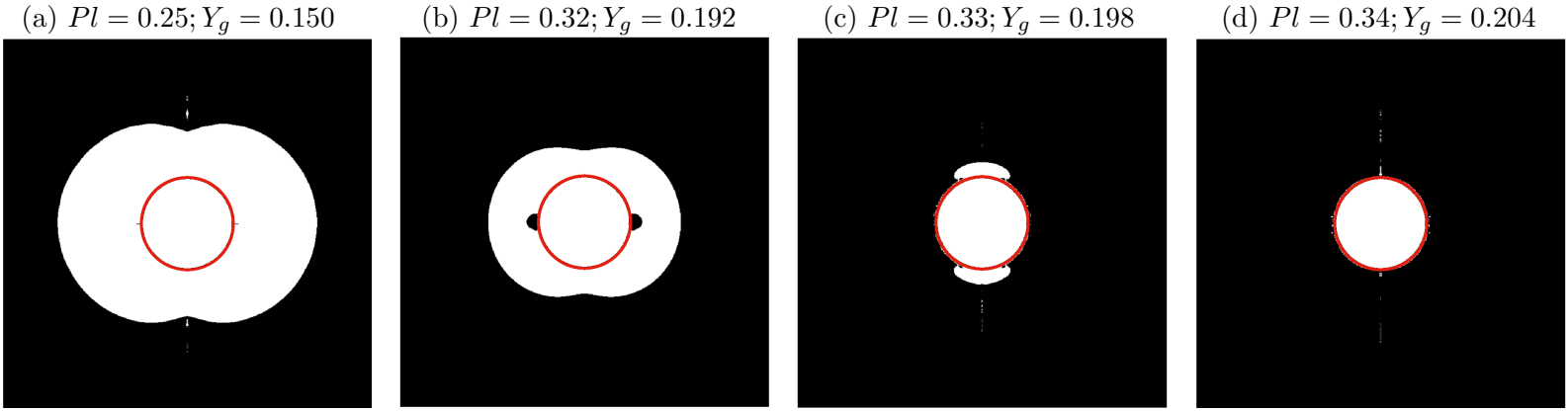

Figure 9: The yielded (white) and unyielded (black) regions around a bubble at $\bar{t} = 0.20$ for different values of Pl. The bubble interface is shown in red color. The other dimensionless parameters are $Ar = 7.5$, $Bo = 0.01$ and $\mu_r = 0.001$.

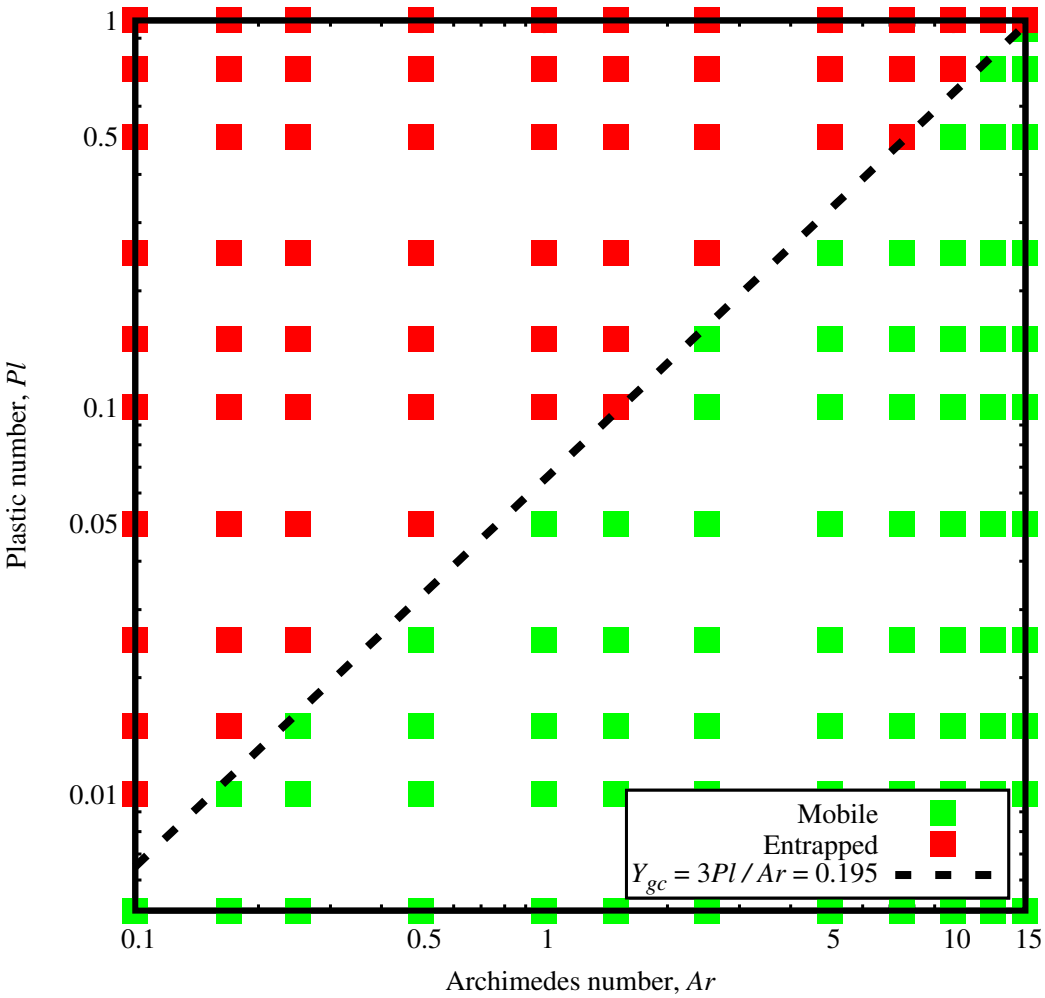

Figure 10: The entrapped and mobile regimes are shown as a function of Pl and Ar for initially spherical bubbles, with $Bo = 1.00$ and $\mu_r = 0.001$. The red and green squares represent the entrapped and mobile regions, respectively. The boundary between the two regimes can be represented by a linear relation $Y_{gc} = 3Pl_c/Ar = 0.195$ shown by the dashed line.

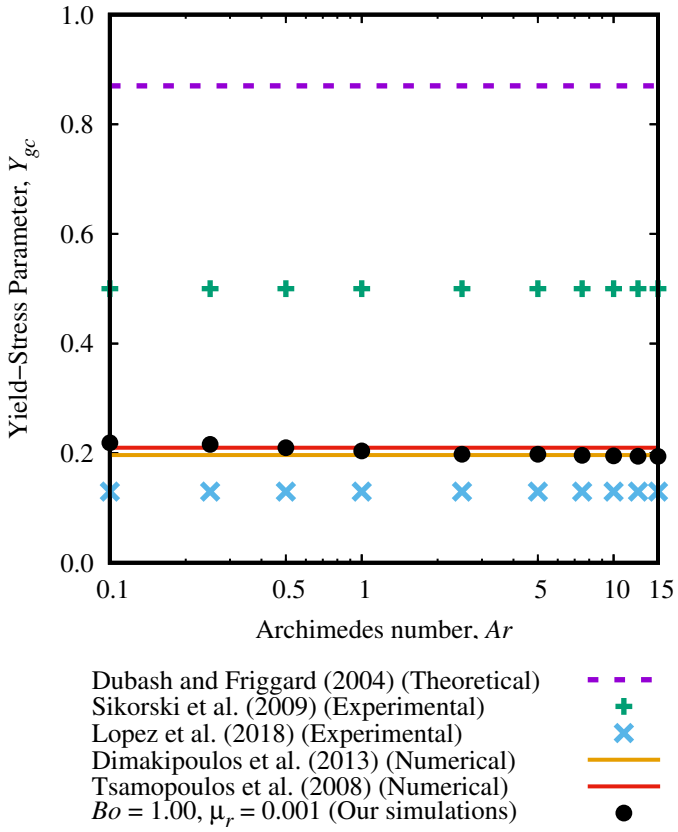

Figure 11: The variation of Y_{gc} with the variation of Ar for $Bo = 1$ and $\mu_r = 0.001$ (black circles). Several values of Y_{gc} reported in different literature is also plotted for a comparison.

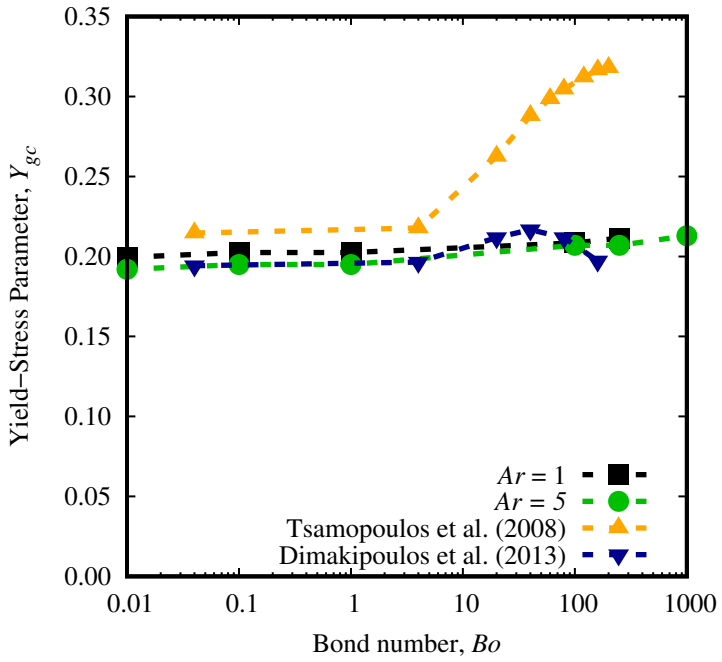

Figure 12: The variation Y_{gc} is plotted with the variation of Bo. Two sets of simulation results are shown ($Ar = 1$ and 5) along with the results of Tsamopoulos et al. (2008) ($Ar \approx 2.24$) and Dimakopoulos et al. (2013) ($Ar \approx 2.37$).

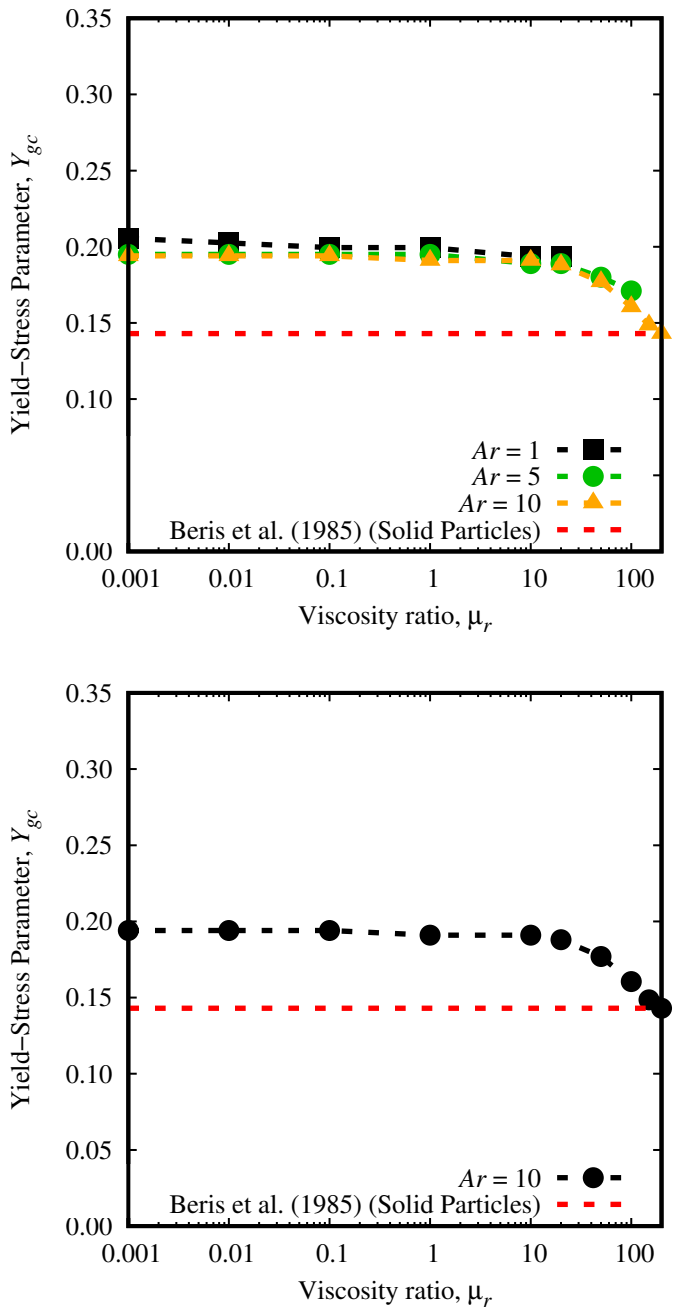

Figure 13: The critial yield stress parameter Y_{gc} is plotted with the variation of μ_r. Three sets of simulation results are shown ($Ar = 1$, 5 and 10) along with the result of Beris et al. (1985) for solid particles ($\mu_r \to \infty$). $Bo = 1$ in all the simulations. The simulations did not converge until $\mu_r = 200$ for $Ar = 5$ and 1. Thus, what figure do you think we should keep, the upper ou lower figure?

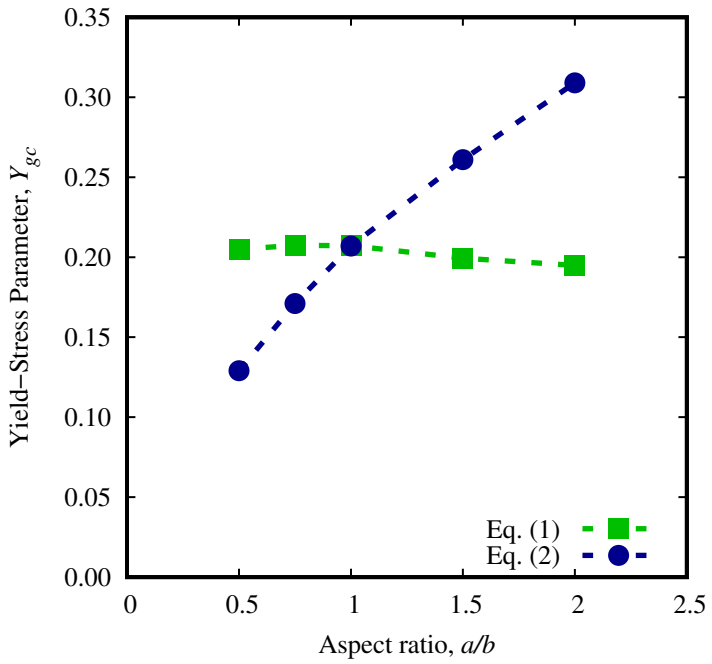

Figure 14: The variation of Y_{gc} with the variation of initial aspect ratio (a/b) of the bubble calculated by Eq. 2 (green line with squares) and Eq. 1 (blue line with circles). The dimensionless parameters are $Ar = 5$ and $Bo = 100$.

(a)

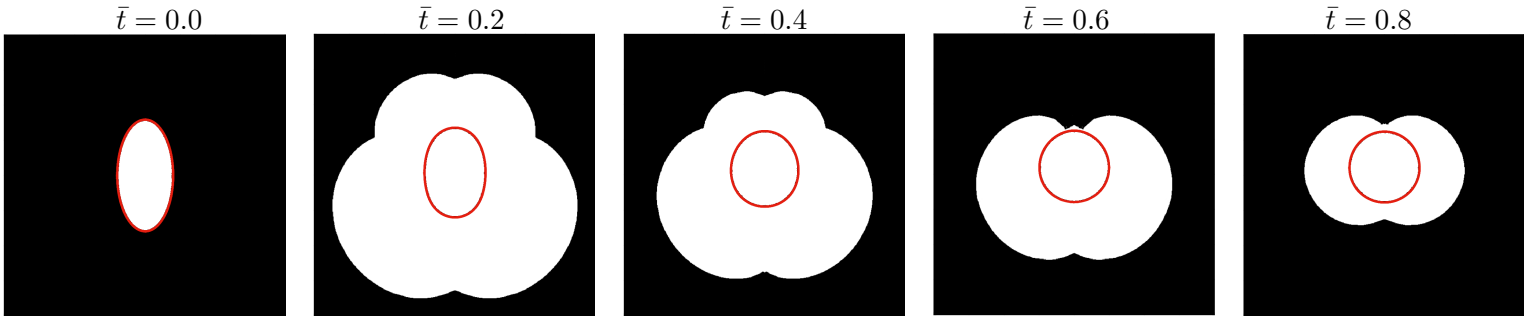
$\bar{t} = 0.0$
$\bar{t} = 0.2$
$\bar{t} = 0.4$
$\bar{t} = 0.6$
$\bar{t} = 0.8$

(b)

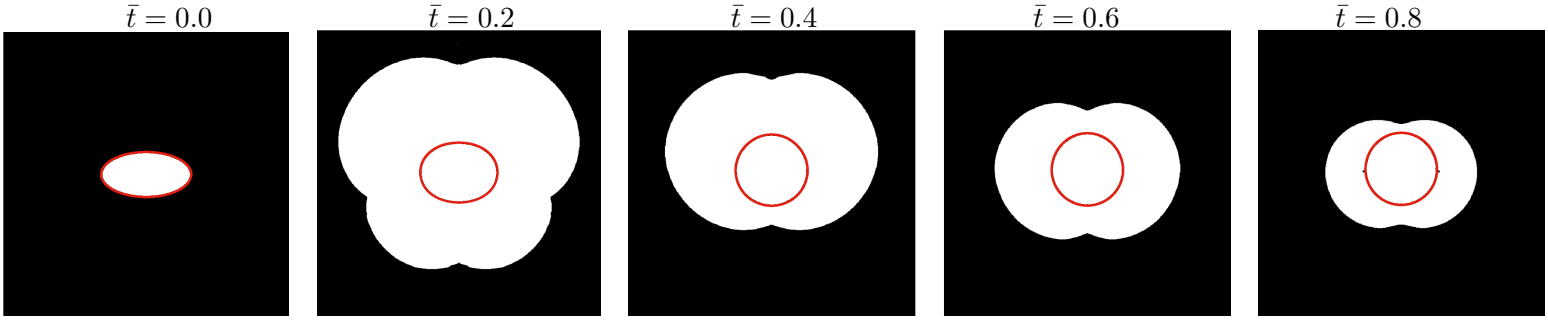
$\bar{t} = 0.0$
$\bar{t} = 0.2$
$\bar{t} = 0.4$
$\bar{t} = 0.6$
$\bar{t} = 0.8$

(c)

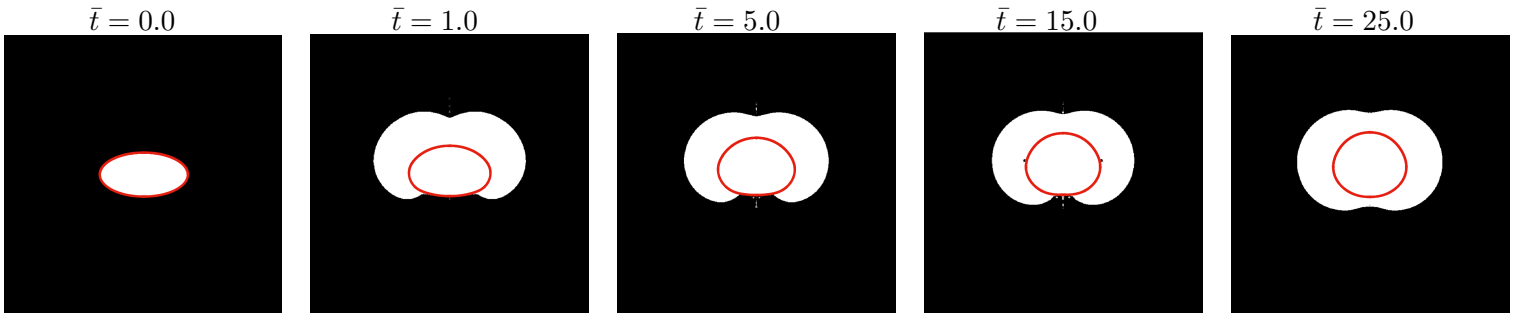

(d)

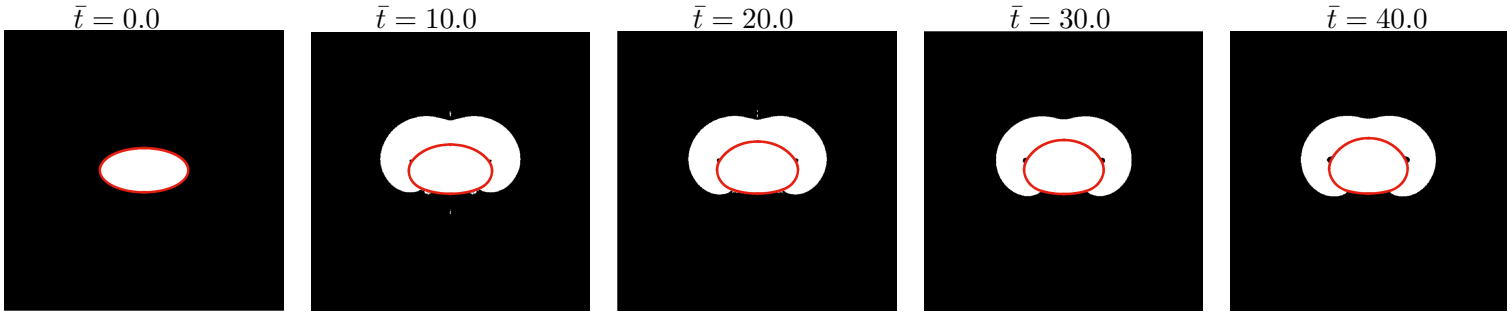

Figure 15: Snapshots of the bubble interface (in red) and yielded (white)/unyielded (black) regions at different times for non-spherical bubbles. Initial aspect ratio of (a) 2.0 and (b) 0.5, $Ar = 5$, $Pl = 0.33$, $Bo = 1$, and $\mu_r = 0.001$. Same results in (c) and (d) for initial aspect ratio of 0.5, $Ar = 10$, $Pl = 0.60$, $Bo = 10$, and $\mu_r = 0.001$ and 10, respectively.

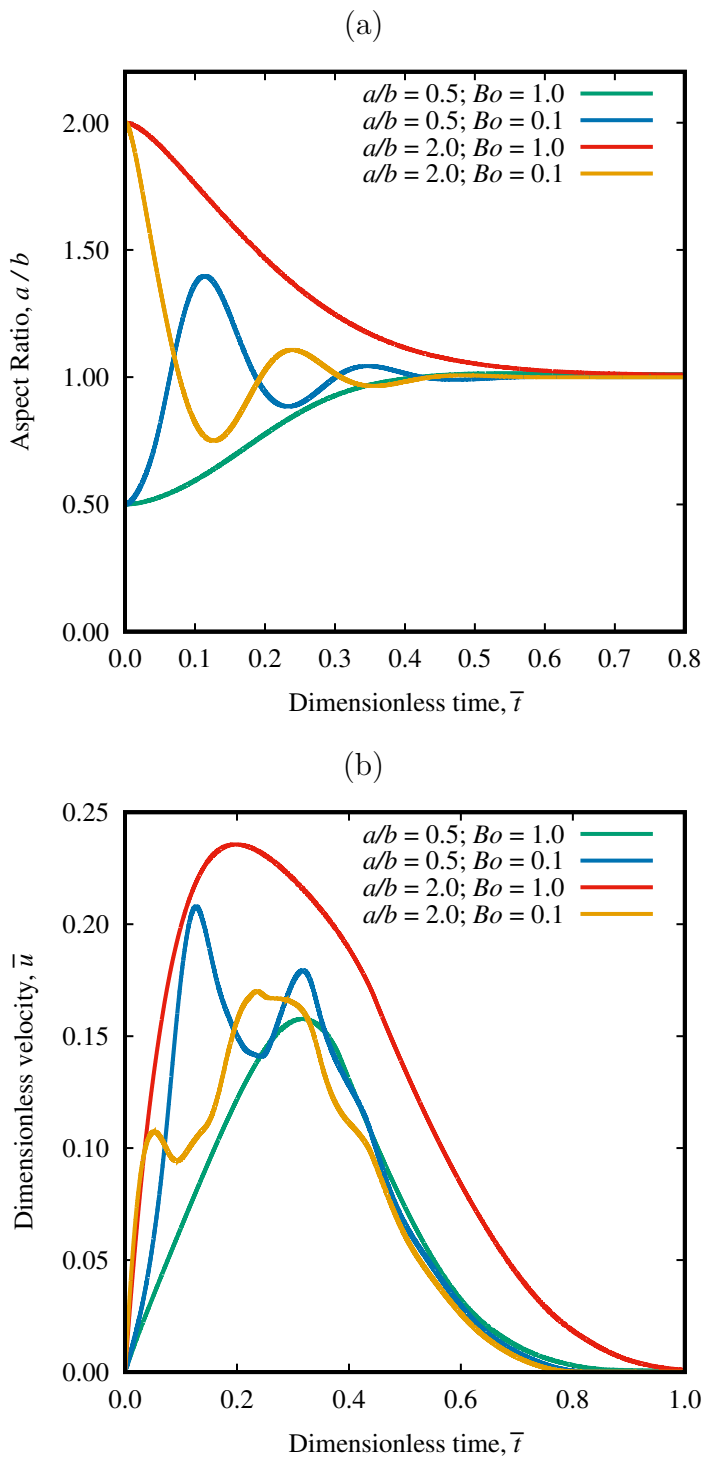

Figure 16: (a)Temporal variation of the aspect ratio of a bubble for different initial shapes and Bond numbers. (b)Temporal variation of the dimensionless rising velocity of a bubble for different initial shapes and Bond numbers. Other dimensionless parameters are $Ar = 5$ and $Pl = 0.33$.

(a)

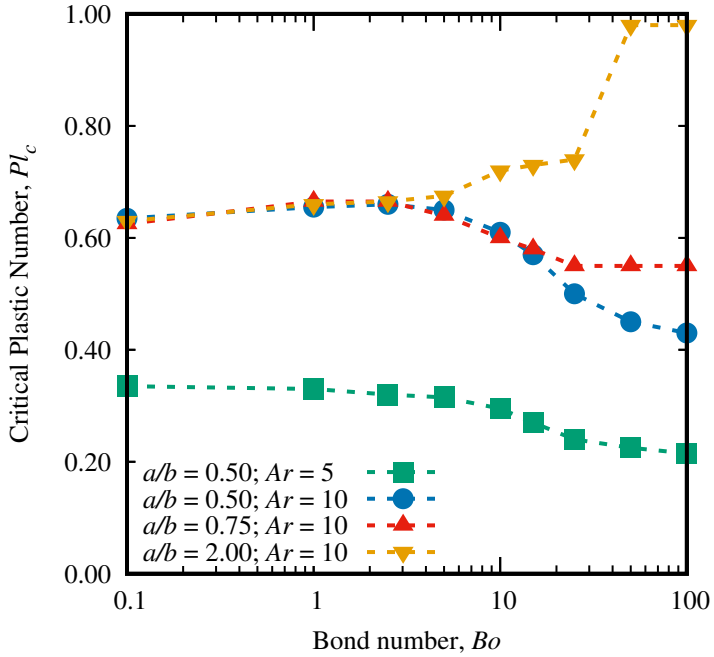
1.00
0.80
0.60
0.40
0.20
0.00
Critical Plastic Number, Pl_c
0.1
1
10
100
Bond number, Bo
a/b = 0.50; Ar = 5
a/b = 0.50; Ar = 10
a/b = 0.75; Ar = 10
a/b = 2.00; Ar = 10

(b)

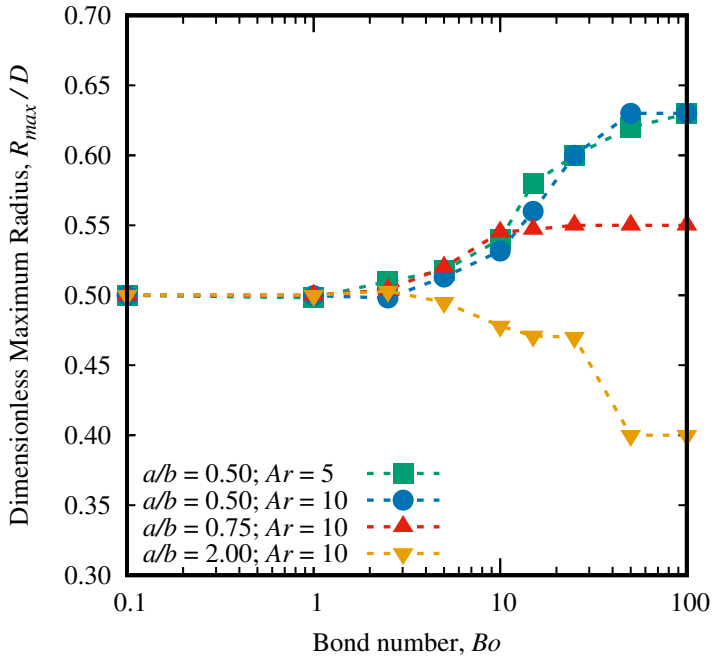
0.70
0.65
0.60
0.55
0.50
0.45
0.40
0.35
0.30
Dimensionless Maximum Radius, R_{max}/D
0.1
1
10
100
Bond number, Bo
a/b = 0.50; Ar = 5
a/b = 0.50; Ar = 10
a/b = 0.75; Ar = 10
a/b = 2.00; Ar = 10

(c)

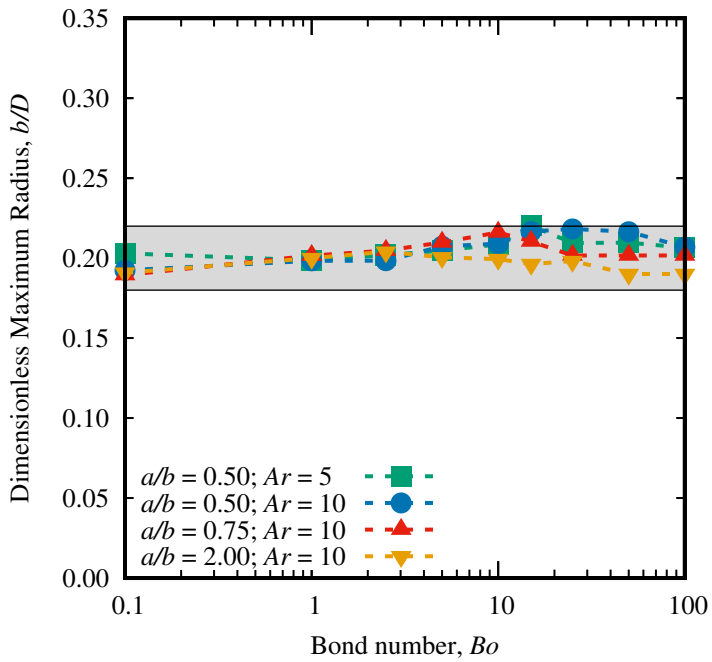

Figure 17: (a) The variation of critical Plastic number with the change Bond number. (b) The radius of the maximum cross-sectional area of the bubble (R_{max}/D) normal to the direction of buoyancy force is plotted for different Bond numbers at the time of entrapment. (c) The variation of the yield stress parameter Y_{gc} (calculated using Eq. (2) with the variation of Bond number Bo. In Eq. (2), R_{max} taken at the time of entrapment as shown in Fig. 17b. The data for two values of Ar (5 and 10), $\mu_r = 0.001$, and different initial shapes ($a/b = 0.50$, 0.75 and 2.00) are plotted together.

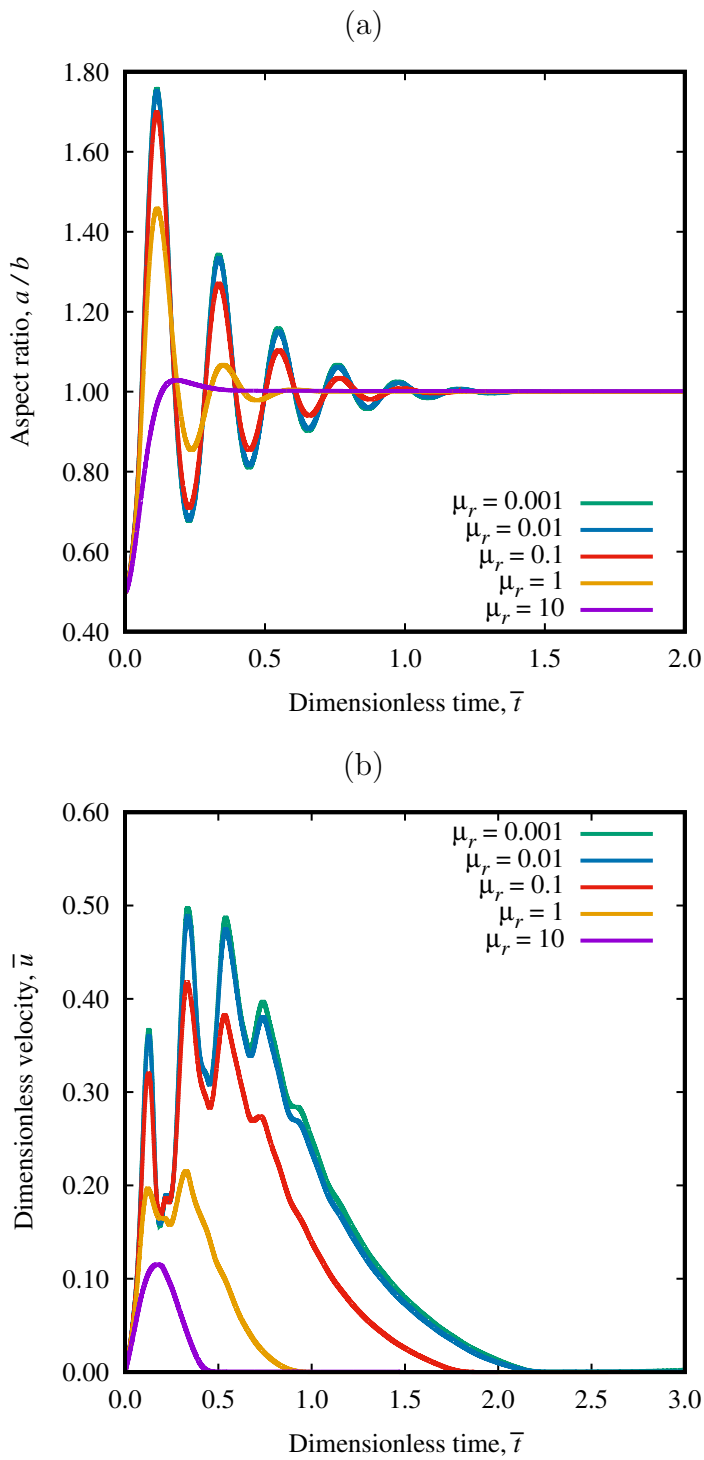

Figure 18: Temporal variation of the (a) aspect ratio and (b) dimensionless rising velocity of a bubble for different viscosity ratios. The dimensionless parameters are $Ar = 10$, $a/b = 0.5$, Bo =0.1 and $Pl = 0.66$.

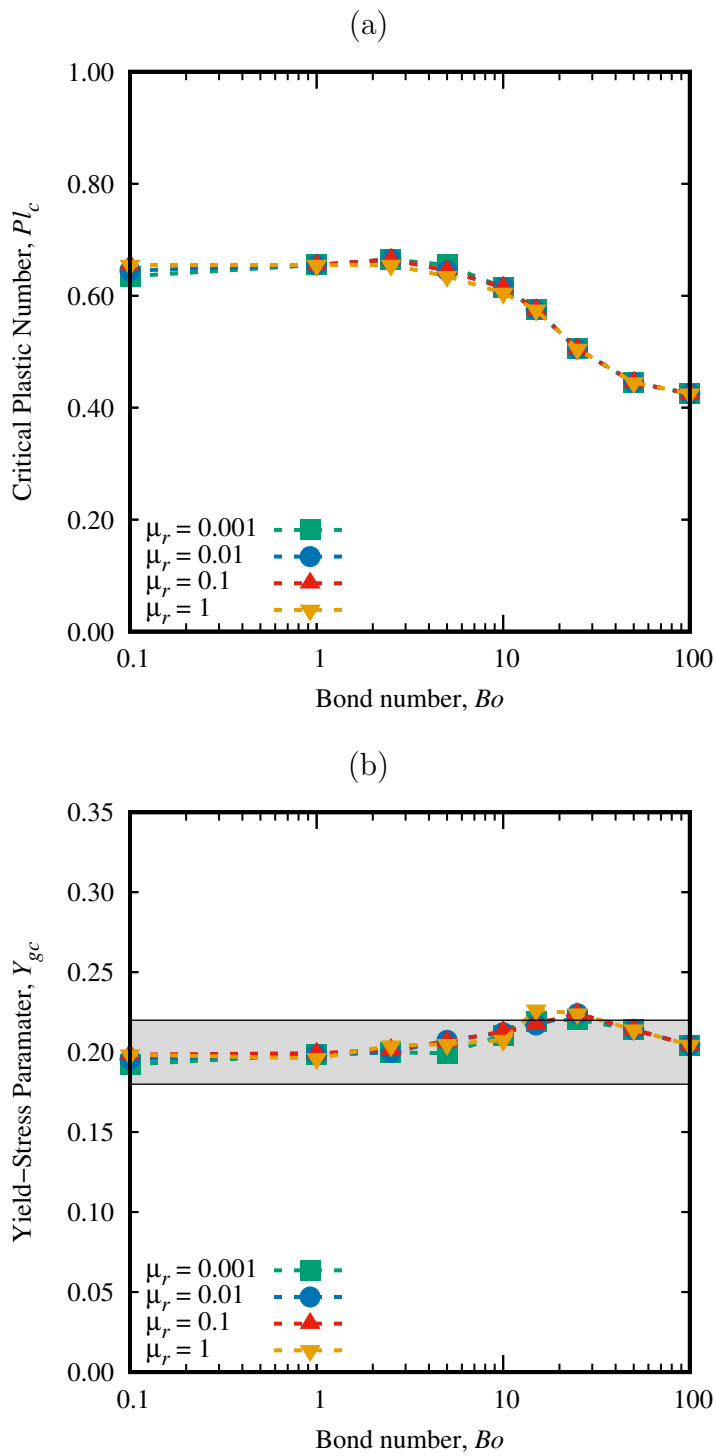

Figure 19: Viscosity ratio effect on the (a) variation of critical Plastic number with the change Bond number and (b) variation of the yield stress parameter Y_{gc} (calculated using Eq. (2) with the variation of Bond number Bo. The dimensionless parameters are $Ar = 10$, $a/b = 0.50$, and $\mu_r = 0.001$, 0.01, 0.1, and 1. (These figures may change too)